Research Square

Preprints are preliminary reports that have not undergone peer review.
They should not be considered conclusive, used to inform clinical practice,
or referenced by the media as validated information.

Solventless, hydrogen-free deoxygenation of palm kernel oil to sustainable aviation fuel precursors over NiSi@Fe3O4 magnetic core-shell catalysts

Alsultan Abdulkareem

kreem.alsultan@yahoo.com

Universiti Putra Malaysia

N. Asikin-Mijan
Universiti Kebangsaan Malaysia

Nawras J. Jassim
Universiti Putra Malaysia

Aqeel Y. Hashim
Universiti Putra Malaysia

M.R. Yusop
Universiti Kebangsaan Malaysia

Salma Samidin
Universiti Kebangsaan Malaysia

H.V. Lee
University of Malaya

Suria Ramli
Universiti Kebangsaan Malaysia

Nur Athirah Adzahar
Universiti Putra Malaysia

Megan X.Y. Ravindran
Universiti Kebangsaan Malaysia

Stella Jovita
Sepuluh Nopember Institute of Technology

Didik Prasetyoko
Sepuluh Nopember Institute of Technology

Mohd Fadly Jumadi
Sime Darby Plantation Research Sdn Bhd

Dai-Viet N. Vo
Trường ĐH Nguyễn Tất Thành

Y.H. Taufiq-Yap

Universiti Putra Malaysia

Research Article

Keywords: Core-shell, cobalt, deoxygenation, magnetic, nickel

Posted Date: May 25th, 2026

DOI: https://doi.org/10.21203/rs.3.rs-9433594/v1

License: This work is licensed under a Creative Commons Attribution 4.0 International License.
Read Full License

Additional Declarations: No competing interests reported.

Solventless, hydrogen-free deoxygenation of palm kernel oil to sustainable aviation fuel precursors over NiSi@Fe_3O_4 magnetic core-shell catalysts

G. AbdulKareem-Alsultan[1,2*], N. Asikin-Mijan[1*],Nawras J. Jassim[1], Aqeel Y. Hashim[1], M.R. Yusop[1], Salma Samidin[1], H.V. Lee[3], Suria Ramli[1], Nur Athirah Adzahar[2], Megan X.Y. Ravindran[1],Stella Jovita[5], Didik Prasetyoko[5], Mohd Fadly Jumadi[4], Dai-Viet N. Vo[6], Y.H. Taufiq-Yap[2]

[1]*Department of Chemical Sciences, Faculty of Science and Technology, Universiti Kebangsaan Malaysia, 43600 UKM Bangi, Selangor Darul Ehsan, Malaysia*

[2]*Catalysis Science and Technology Research Centre (PutraCat); Faculty of Science, Universiti Putra Malaysia, 43400 UPM Serdang, Selangor, Malaysia.*

[3]*Nanotechnology and Catalysis Research Centre (NanoCat), Institute of Postgraduate Studies, University Malaya, 50603 Kuala Lumpur, Malaysia*

[4]*Plantation Fadlly Jumadi, Sime Darby Plantation Research Sdn Bhd, Oils and Fats Processing Technology, Carey Island Selangor*

[5]*Department of Chemistry, Faculty of Science and Data Analytics, Institut Teknologi Sepuluh Nopember (ITS), Sukolilo, Surabaya 60111, Indonesia*

[6]*Institute of Applied Technology and Sustainable Development, Nguyen Tat Thanh University, Ho Chi Minh City 755414, Vietnam*

[*]Corresponding authors: nurul.asikin@ukm.edu.my; kreem.alsultan@yahoo.com

Abstract

The production of sustainable aviation fuel (SAF) has been improving for the past few years. In Malaysia, palm-based biomass is the focus of this study for the production of SAF due to its abundant supply. Indeed, the SAF from palm kernel oil (PKO) is produced through deoxygenation (DO) reaction via decarboxylation/decarbonylation (deCOx) pathways using a series of magnetic core-shell catalysts (NiSi@Fe_3O_4, CoNiSi@Fe_3O_4 and MoNiSi@Fe_3O_4) under H_2-free atmosphere. In general, DO activity was predominated by CoNiSi@Fe_3O_4 and yielded liquid hydrocarbons of 75% with 85% bio-jet fuel, owing to the existence of rich Lewis acid sites that cause more C = O and C–O groups to bond preferentially on the Co site. Ni favours cracking and hydrodeoxygenation (HDO) reactions due to rich Bronsted acid sites. The deactivation kinetic study confirms that the deactivation happens by the coke formation and flow of second-order deactivation. An amorphous (C_β) and graphitic (C_c) carbon phase are the major types of coke detected on used CoNiSi@Fe_3O_4 at DO temperatures within 300–350 °C. The rate of graphitization increases in direct proportion to the rise in DO reaction temperature.

Keywords: Core-shell, cobalt, deoxygenation, magnetic, nickel

Introduction

Earth is likely to cross a critical threshold for global warming within the next decade as the world continues to burn planet-warming fossil fuels like coal, oil and gas. And that trend shows no sign of slowing. According to a new update issued by the World Meteorological Organization (WMO) that between 2023 and 2027, there is now a 66% chance that the planet's temperature will increase above 1.5 degrees Celsius of warming above pre-industrial levels for at least one year [1]. Indeed, NASA has reported that the Arctic is warming much faster than other regions on Earth; the global sea level has risen about 3.9 inches since 1993. Indeed, the National Geographic believed that this extraordinary pace of glacier melting, which resulted in the rising of sea level, was the reason for the occurrence of destructive weather phenomena (hurricanes and typhoons), which caused massive death tolls [2]. In May 2023, the National Coastal Erosion Study reported that without any necessary intervention, Malaysia, as a maritime nation, is at risk of losing 1,350 km of coastline to severe erosion due to global warming in the next few years [3]. Due to the aforementioned facts, many researchers have made attempts to mitigate the aggravating effects of global warming, one of which is reducing greenhouse gas (GHG) emissions associated with fossil fuel usage. This has led to various government programmes promoting biofuels.

Sustainable aviation fuel (SAF), derived from biomass and waste-based feedstocks, offers the capability to achieve performance comparable to conventional petroleum-derived jet fuel while significantly reducing overall carbon emissions. One common production route for SAF involves the catalytic deoxygenation (DO) of fatty acids, a process in which oxygen-containing functional groups—specifically carboxyl and carbonyl groups—are removed through decarboxylation and decarbonylation (deCOx) pathways. These reactions release CO_2 or CO and result in the formation of linear hydrocarbons with a carbon chain length reduced by one atom relative to the original fatty acid [4]. DO offers a cleaner catalytic process compared to hydrotreating due to its solventless and H_2-free reaction system. It has been investigated that cheaper transition metal oxides such as Ni, Fe, Mo, Co, Cu, and W-promoted catalysts have been successfully employed as effective metal-promoted catalysts in DO reactions for the production of gasoline, diesel, and SAF; indeed, those catalysts exhibited superior performance with hydrocarbon yields of 80–97% [5–7]. Noteworthy to mention is that Ni has been demonstrated to be a good choice as an active component for the DO reactions. Indeed, the existence of rich Ni^{2+}/Ni^0 was found to be remarkably active in cracking, which is thus efficient in driving hydrogenation of alkenes and selective toward alkanes [8]. In fact, it is expected that this will enhance SAF's winterization properties. Particularly,

Ni-rich formulations tend to promote excessive cracking, resulting in a higher yield of gaseous products [9]. To date, Ni/Al_2O_3 catalysts have been widely applied in deoxygenation (DO) reactions. However, a major limitation of Ni-based catalysts is their susceptibility to sintering and carbon deposition, which leads to

catalyst deactivation [10]. To address these challenges, previous studies have investigated the modification of Ni with carbon-resistant active species, such as cobalt, to enhance catalyst stability and performance [8] and cobalt doping of nickel catalysts was found to improve Ni reducibility, allow an increase in hydrogen uptake, and thereby boost the alkane products. It's noteworthy that the Ni-Co catalyst has been shown to have a synergistic impact that can increase DO activity even at low temperatures [11]. However, this kind of catalyst was reported to be easily deactivated due to coking.

Noteworthy, core-shell metal catalysts are one of the ideal alternatives to retard sintering of metal as the active metal is uniformly distributed on the support shell, in which the metal particle cannot move outside the support shell due to the larger size of the support pore, hence simultaneously inhibiting the gathering of metal active sites [12]. Magnetic oxide is proven to be an effective catalyst with an easy separation feature for the DO reaction [13]. However, catalytic activity of Fe_3O_4 might decrease because the Fe_3O_4 core is generally unstable, susceptible to corrosion, and easy to agglomerate [14]. It has been observed that the SiO_2 layer prevents sintering at high temperatures and protects and stabilizes the Fe_3O_4 core, thereby sustaining the magnetism properties of Fe_3O_4. Noteworthy, Kamzin suggests that the SiO_2 shell provides a chemically inactive surface that prevents the leaching of particles in an acidic solution [15]. The introduction of bimetal oxides into the Si framework has been proven to be the most active and selective catalyst in many thermal catalytic processes [16,17], owing to the synergetic effect of bimetal and Si support. Nevertheless, the synergistic effect of CoNi on the magnetic Si framework (Si@Fe_3O_4) remained ambiguous.

Although numerous studies have explored the production of SAF via deoxygenation (DO), its large-scale utilization and industrial implementation remain insufficiently investigated [18,19]. This is because the price of SAF feedstock is considered a barrier to large-scale production of SAF to meet global competition. Malaysia, as one of the world's leading palm oil producers and exporters of palm oil (PO) and palm kernel oil (PKO), recognises that PKO is an ideal SAF feedstock, and several Malaysian researchers have admitted that the SAF obtained from DO PKO is compatible with the Jet A-1 commercial fuel standard [20,21]. This is due to the main fatty acid composition of PKO, which comprises C_{12}-C_{16} fatty acids, in which the effective DO of PKO typically yields bio-jet fuel-range hydrocarbons (C_{10}-C_{16}). Indeed, utilisation of real feedstock like PKO is challenging in the DO process, especially in catalyst deactivation studies; nevertheless, deep studies on the deactivation process in catalytic DO using PKO are still lacking, which most researchers neglected. For instance, severe deactivation, including metal sintering, thermal degradation of the support, and coke deposition, are unavoidable phenomena during the DO process. The relevance of each deactivation cause depends on catalyst composition, structure, and operating conditions (most common is temperature) [6]. Due to this reason, the aims of this work were to investigate the real reason for catalyst deactivation in catalytic DO of PKO using a magnetic core-shell catalyst (CoNi Si@Fe_3O_4). The type of catalyst deactivation was determined by examining the effects of reaction time on product yield and catalyst deactivation using both

zero and non-zero asymptote rates. Before focusing on the deactivation CoNiSi@Fe_3O_4 DO study, screening catalytic studies were carried out using NiSi@Fe_3O_4 and MoNiSi@Fe_3O_4 catalysts.

Experimental

Preparation of core-shell structured and supported magnetic Fe_3O_4 catalysts

Ferrimagnetic Fe_3O_4 particles were first synthesised by the co-precipitation of $FeCl_2.4H_2O$ and $FeCl_3.6H_2O$, (Sigma-Aldrich, ≥99.0 %). The Fe^{3+} and Fe^{2+} salts were dissolved in deionised water in a 2:1 molar ratio and stirred at 40 °, prior to the dropwise addition of 28 vol% NH_3 (Riedel-de Haen) until the pH increased to 11. The resulting nanoparticulate sediment was filtered and vacuum-dried at 60 °C for 24 h. A sol-gel method was used to prepare the Si@Fe_3O_4 core-shell material. Approximately 0.5 g of Fe_3O_4 nanoparticles was uniformly dispersed in 200 mL of ethanol (Aldrich, 99%) using ultrasonication at room temperature for 15 min. Subsequently, 10 mL of 28 vol% NH_3 solution and 18 mL of deionised water were added. The mixture was then stirred with 1 mL of 98% tetraethyl orthosilicate for 4 h. The resulting particles were collected by filtration, washed with ethanol and deionised water, and finally vacuum-dried at room temperature. The introduction of metal dopants to 0.2 g of the preceding core@shell material was achieved by co-precipitation using 10 wt% Ni, Co and Mo (0.68M Ni^{2+} 0.6M Co^{3+} and 0.6M Mo^{6+}) as their nitrate ($Co(NO_3)_2.6H_2O$; ($Ni(NO_3)_2.6H_2O$, Sigma Aldrich, ~99 %) or ammonium heptamolybdate tetrahydrate ($(NH_4)6Mo_7O_{24}.4H_2O$, 99 %) salts. Ammonia solution was added to raise the pH to 11, the resulting suspensions stirred for 2 h, and the precipitate filtered and dried overnight at 120 °C prior to calcination for 3 h at 550 °C. The resulting materials were denoted Fe_3O_4, Si@Fe_3O_4, NiSi@Fe_3O_4, NiCoSi/Fe_3O_4 and NiMoSi/Fe_3O_4, respectively.

Catalyst characterisation

The chemical composition of the materials was determined using X-ray fluorescence (XRF) spectroscopy with a scandium anode (PHILIPS PW1404), while crystalline phases were identified by X-ray diffraction (XRD) on a Shimadzu XRD-6000 instrument employing Cu Kα radiation at 30 kV. Textural properties, including surface area and pore size, were analyzed using a Micromeritics ASAP 2020 porosimeter based on the Brunauer–Emmett–Teller (BET) and Barrett–Joyner–Halenda (BJH) methods. Prior to analysis, samples were degassed at 150 °C for 4 h to remove moisture, followed by N_2 adsorption–desorption measurements at −196 °C.

Acidic characteristics were evaluated via temperature-programmed desorption (TPD) using a Micromeritics AutoChem II+ chemisorption analyzer equipped with a thermal conductivity detector (TCD). Approximately 0.05 g of sample was pretreated under flowing N_2 at 150 °C for 1 h, then saturated with NH_3 for about 1 h at room temperature. The system was subsequently purged with N_2 (20 mL/min) for 1 h. Desorption of adsorbed NH_3 was monitored by TCD under a helium flow (30 mL/min) while heating the sample from 50 to 700 °C at a rate of 10 °C/min.

Catalyst morphology was examined using a LEO 1455 VP field-emission scanning electron microscope (FE-SEM) operating at 20 kV, and magnetic properties were measured with an ADE EV-7 vibrating sample

magnetometer (VSM). Coke deposition was investigated through temperature-programmed oxidation (TPO) under a flow of 30 mL/min of 5 vol% O_2/He, with a heating rate of 10 °C/min. Raman spectra were collected using a Horiba Jobin–Yvon LabRAM spectrometer coupled with an Olympus confocal microscope (×100 objective), equipped with a Peltier-cooled CCD detector. A 532 nm excitation wavelength from a diode-pumped solid-state laser (Spectra-Physics) was used, with a laser power of 30 mW.

Catalytic reaction testing

PKO was obtained from Sime Darby Oils kernel crushing plant located on Carey Island. The fatty acid composition of PKO was determined by their transformation into fatty acid methyl ester (FAME). Palm kernel oil (PKO) exhibited a low free fatty acid content (FFA: 0.85–0.9 wt.%). Transesterification was carried out in methanol using KOH as a homogeneous base catalyst, with a methanol-to-oil ratio of 1:15, at 65 °C for 3 h. The fatty acid compositions of both untreated PKO and the resulting FAME products were determined by GC–MS (Table 1), revealing lauric acid (C12:0, 48%) as the predominant component, followed by myristic acid (C14:0, 16%), oleic acid (C18:1, 15%), and palmitic acid (C16:0, 8%) [22,23]. Catalytic deoxygenation (DO) of PKO was performed in a mechanically stirred 250 mL semi-batch reactor. Approximately 10 g of PKO and 5 wt.% catalyst were introduced into the reactor under a continuous N_2 flow of 20 mL/min to remove residual air. The system was then heated at a rate of 10 °C/min under the same N_2 atmosphere to the target reaction temperature and maintained for 3 h. Volatile products were condensed from the outlet stream at 19 °C, while gaseous products were collected in a 1 L gas bag. Liquid products were analyzed using GC–FID and GC–MS, whereas gaseous products were analyzed by GC–TCD. All experiments were conducted in triplicate to ensure reproducibility.

Table 1. The physicochemical properties and fatty acid composition of PKO.

Properties	**Value[a]**	**Value[b]**	**Method**
Acid value (mg KOH/g)	3.4	2.7±0.3	AOCS Ca 5a-40
FFA	1.7	1.35 ±0.15	AOCS Ca 5a-40
Kinematic viscosity at 40 °C (mm/s)	35.3	4.42	EN ISO3104
Density (kg/m^3)	0.88	0.86 – 0.9	D1298
Fatty acid composition (%)[b]			
Lauric acid ($C_{12:0}$)	48.0		
Oleic acid ($C_{18:1}$)	15.4		
Palmitic acid ($C_{16:0}$)	8.0		
Caprylic acid ($C_{8:0}$)	3.0		AOCS Ce1-62 & Ce-661
Capric acid ($C_{10:0}$)	4.0		
Myristic acid ($C_{14:0}$)	16.0		
Other[c]	5.5		

[a]Experimental value; [b]Literature value; [22,23] [c]Total FFA for stearic acid ($C_{18:0}$), arachinoic acid ($C_{20:0}$).linoleic acid ($C_{18:2}$),

Product analysis

Gas chromatography using a flame ionisation detector (GC-FID) (Shimadzu GC-14B) and an Agilent J&W HP-5 capillary column (column specifications: film thickness: 0.25 mm, length: 30 m and inner diameter: 0.32 mm) operating at 300 °C was used to identify and quantitatively evaluate the GC-grade n-hexane from Sigma Aldrich USA was used to dilute the deoxygenated liquid products. Before analysing the yield, the liquid product was diluted . For the purpose of quantitative analysis, 1-bromohexane (CHBr from Sigma Aldrich USA) was used as an internal standard. The GC column was injected with a 1 mL aliquot of the sample. The temperature of the injection was 250 °C. The carrier gas used in this instance was nitrogen. The oven was preheated to 40 °C and maintained at that temperature for 6 min before being gradually heated to 270 °C at a rate of 7 °C.min^{-1}. Catalytic performances were evaluated through the yield obtained of subjected products (saturated and unsaturated straight-chain hydrocarbons) using **Eq. 1**.

$$x(\%) = \left(\frac{mol\ TG\ in\ feed - mol\ TG\ in\ product}{mol\ TG\ in\ feed}\right) \times 100 \qquad Eq.1$$

$$Y(C_8 - C_{20}, \%) = \left(\frac{Total\ mol\ of\ n - Alkanes(C_8 to\ C_{20}\ in\ product}{Total\ mol\ of\ fatty\ acid\ in\ feed}\right) \times 100 \qquad Eq.2$$

GC-MS (Shimadzu QP5050A) fitted with a non-polar DB-5HT column (column specifications: 0.32 ×30 m mm×0.25 mm) with split-less inlet was used to qualitatively describe the product distribution of the

deoxygenized liquid product. n-hexane of GC grade (>98%) was used to dilute the samples to a concentration of 100 ppm. The National Institute of Standards and Testing library was used to identify the generated fraction peaks from the GC-MS spectra. The compound identification was based on a potential match of 95% or above. Eq. 3 was used to calculate the selectivity of the organic product, which included hydrocarbon fractions, carboxylic acid, alcohol, and other components.

$$S_{product} = \frac{C_y}{\sum n_y} \times 100\% \quad (3)$$

where, $S_{product}$ = yield/selectivity of organic compound (diesel range product)n (%), C_y = area of the desired organic compound(n-Cx), n_y = total area of organic compounds.

Reaction kinetics

To determine the kinetics of the reaction, the effects of reaction temperature and time were measured. Furthermore, to explain the rate of kinetic energy, the activation energy needs to be determined. The overall activation energy required for the DO of PKO was determined using the Arrhenius rate law, Eq. 4.

$$InK_{app} = InA - \frac{E_a}{RT} \quad (4)$$

where K app denotes the apparent rate constant of the reaction (s^{-1}), and (A) represents the pre-exponential (frequency) factor, reflecting the frequency of collisions between reactant molecules regardless of their kinetic energy (s^{-1}), . (Ea) is the activation energy E_a , and (T) is the absolute temperature K.

In addition, the thermodynamic parameters were evaluated using transition-state theory (TST), which describes the activation process in terms of key thermodynamic quantities, including the entropy of activation ΔS, enthalpy of activation ΔH, and Gibbs free energy of activation ΔG. The Eyring equation, derived from TST, is presented in Eq. (5). can be written as [27].

$$In\left(\frac{K_{app}}{T}\right) = -\frac{\Delta H^{\#}}{R} + In\left(\frac{K_B}{h}\right) + \left(\frac{\Delta S^{\#}}{R}\right) \quad (5)$$

where, K_{app} is the apparent rate constant (s^{-1}), ΔH#is the activation enthalpy, ΔS is the entropy of activation, and K_B and h are the Boltzmann and Planck constants, respectively.

Deactivation study

The power-law equation provided below can be applied to the time stream results in order to determine the deactivation rate for each reaction (Eq. 6 & Eq.7);

$$-r_{dec} = {}^{da}/_{dt} = k_{dec}a^d \quad (6)$$

$$-r_{dec} = k_{dec}\left[\frac{1}{1+ k_{dec}t^m}\right]^d \quad (7)$$

where (a) represents the relative rate, defined as the ratio of paraffin yield at time (t) to the initial paraffin yield at (t = 0); (kdec) is the deactivation rate constant; (d) denotes the deactivation order ((d = 1, 2, or 3));

and (m) is the fouling parameter. This type of deactivation behavior is commonly observed in hydrocarbon reactions, where carbonaceous deposits (coke) accumulate on the catalyst surface, resulting in catalyst deactivation [6].

Eq. 8 used to determine the zero-asymptote rate, employing a classical first-order deactivation model. This model assumes that, as the catalyst remains on stream for an infinitely long time, the rate will gradually approach zero asymptotically. The integrated form of this model is illustrated in Eq. 9.

$$\frac{da}{dt} = -k_d Da \; ; \; a = \frac{r(t)}{r_0} \tag{8}$$

$$r(t) = e^{-k_d t} r_0 \tag{9}$$

where (r_0) is the initial reaction rate and (k_d) is the deactivation constant. These parameters must be determined through fitting, which can be achieved using the SOLVER add-in to minimize the sum of squared deviations [24].

Eq. 10 used to compute the non-zero asymptote rate using a first-order deactivation model. It can be assumed that, as the catalyst remains on stream for an infinitely long time, it will approach a steady state rate asymptotically. The integrated form of this model is illustrated in Eq. 11.

$$\frac{da}{dt} = -k_d(a - a_{ss}); \; a = \frac{r(t)}{r_0} \; ; \; a_{ss} = \frac{r(t\to\infty)}{r_0} \tag{10}$$

$$r(t) = e^{-k_d t} (r_0 - r_{ss}) + r_{ss} \tag{11}$$

where (r_0) represents the initial rate, (k_d) is the deactivation constant, and (r_{ss} denotes the steady-state rate. These three parameters must be estimated through fitting, which can be performed using the SOLVER add-in to minimize the sum of squared deviations.

Results and discussion

Physicochemical characterisation

The presence of crystalline phases was examined by powder XRD (**Fig. 1a**) All catalysts exhibited reflections consistent with the (220), (311), (400), (422), (511), and (440) planes of cubic Fe_3O_4 (ICDD Card No. 00-002-1047), and hence anticipated to exhibit ferrimagnetism at room temperature. Silicon addition had negligible impact on the parent Fe_3O_4 diffractogram, and no crystalline silica phases were observed for any catalysts indicating amorphisation or sub-2 nm crystallites [25]. For Ni modified catalysts, additional reflections associated with (202) and (220) planes of cubic NiO were observed at 33.1°, 54°, and 64.5° (ICDD Card No: 00-001-1239), alongside those for hematite Fe_2O_3 at 24.1° and 40.9° (ICDD No: 00-001-1053) possibly resulting from partial oxidation of Fe_3O_4 during re-calcination. CoNiSi@Fe_3O_4 exhibited weak

reflections characteristic of the (220), (311), (511), (440) planes of cubic Co_3O_4 (ICDD Card No: 00-001-1152) whereas no reflections attributable to crystalline MoO_x phases were detectable for MoNiSi@Fe_3O_4. Volume-averaged crystallite sizes of the Fe_3O_4 phase determined by Scherrer analysis of the (311) reflection ranged between 6 and 18 nm (**Table 2**). The composition of all catalysts was dominated by iron, with the presence of Si in all Si@Fe_3O_4 catalysts consistent with the encapsulation of Fe_3O_4 nanoparticles with a silicate shell. For Ni modified Si@Fe_3O_4, the Ni loading spanned 8-23 wt%, while CoNiSi@Fe_3O_4 and MoNiSi@Fe_3O_4 contained 20.5 wt% Co and 2.4 wt% Mo respectively.

Textural properties were examined by N_2 physisorption (**Fig. 1b**), with all catalysts exhibiting type-IV isotherm with hysteresis loops for $p/p_0 > 0.4$, indicative of large mesopores [26]. Surface areas and pore volumes of modified Fe_3O_4 catalysts were lower than the parent values (**Table 2**) but showed no systematic variation. Mesopore diameters were ~10 nm in all case.

Table 2. Physical properties of catalysts.

Catalyst	**Elemental analysis[a] wt%**					**Crystallite size[b] / nm**	**BET[c] / m^2g^{-1}**	**Pore size[c] / nm**	**V_p[b] / $cm^3.g^{-1}$**
	Fe	**Si**	**Ni**	**Co**	**Mo**				
Fe_3O_4	98.2	-	-	-	-	14	80	9	0.22
Si@Fe_3O_4	82.1	17.7	-	-	-	10	47	11	0.14
NiSi@Fe_3O_4	62.7	14.1	23.1	-	-	18	53	12	0.18
CoNiSi@Fe_3O_4	54.0	14.2	11.2	20.5	-	6	66	9	0.16
MoNiSi@Fe_3O_4	74.9	13.8	8.4	-	2.4	9	44	11	0.13

[a]XRF; [b]XRD; [b]BET surface area; [c]BET method.

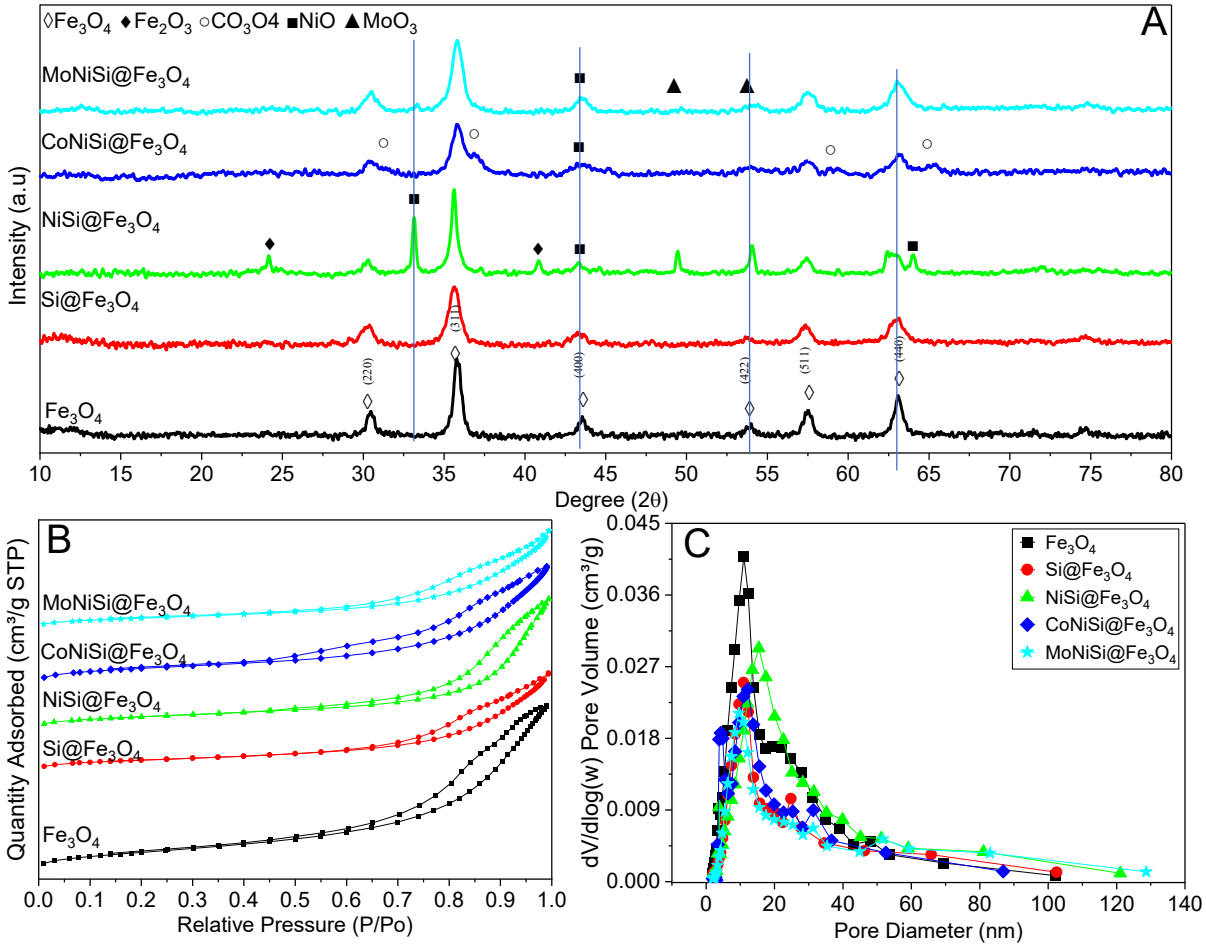


Fig. 1. (a) Powder XRD diffractograms, (B) N_2 adsorption-desorption isotherms, and (C) pore size distributions determined by the BJH method for Fe_3O_4 containing catalysts.

Catalyst morphology was further examined by FE-SEM (**Fig. 2**). The parent Fe_3O_4 comprised agglomerates of uniform spherical particles of ~15 nm diameter (**Fig. 2a**). Si modification results in larger and smoother spherical particles with a broader size distribution and mean diameter ~38 nm (**Fig. 2b**). Subsequent modification of Si@Fe_3O_4 by Ni (**Fig. 2c**) and Co (**Fig. 2d**) had little impact on particle morphology, however Mo addition to NiSi@Fe_3O_4 (**Fig. 2e**) produced a flower-like architecture with thin, interconnected platelets similar to sand roses observed for layered double hydroxides. Similar findings were reported by Botas's study, whereby, based on their TEM findings, the Mo species was found to be widely distributed and located mainly within the catalyst support (zeolitewas in agreement with Gyawali and Hae's research study, which showed a series of Mo-modified catalysts with a flower-like structure via a hydrothermal approach [27]. Noteworthy, low Mo species on catalyst surface were detected by XRF. Indeed, no detection of Mo species by FESEM-EDX analysis probably due to below detection limit. It) channels rather than on the external surface of the zeolite [28].

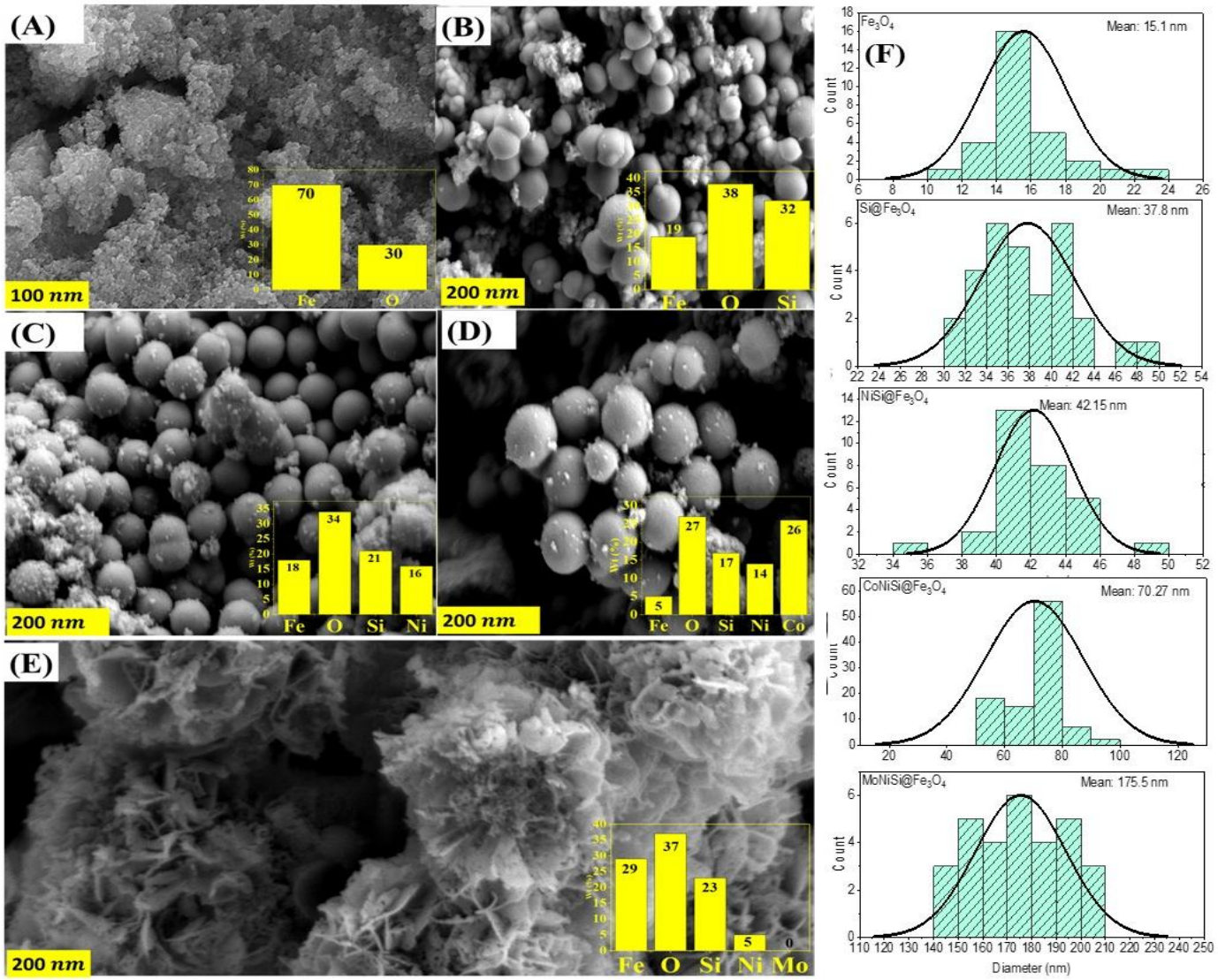


Fig. 2. FE-SEM images and EDX analysis of (A) Fe_3O_4, (B) Si@Fe_3O_4, (C) NiSi@Fe_3O_4, (D) CoNiSi@Fe_3O_4, and (E) MoNiSi@Fe_3O_4 catalysts and (F) their corresponding particle size distributions.

Acid properties were investigated by ammonia chemisorption and subsequent TPD (**Fig. 3**). All catalysts exhibited multiple desorption peaks with peak maxima temperatures falling in the ranges 100-200 °C, 200 °C < T < 450 °C, and >450 °C, arising from weak, medium and strong acid sites, respectively [29,30]. Fe_3O_4 and NiSi@Fe_3O_4 possessed the highest loading of strong acid sites (~1,100 μmol.g^{-1}, **Table 3**), however the proportion of strong acid sites decreased in the order: CoNiSi@Fe_3O_4 > Fe_3O_4 > MoNiSi@Fe_3O_4 ≈ NiSi@Fe_3O_4 > Si@Fe_3O_4. According to [31], Lewis acidic sites are desirable for fuel DO and yielding rich hydrocarbons with an odd number of carbon atoms compared to their parent fatty acid, while the strong acidic sites are mainly responsible for the cracking reaction and yielding rich light fraction species. It should be emphasised that rising Lewis acidity, as opposed to its Bronsted acid counterpart, will aid in growing coking resistance [32].

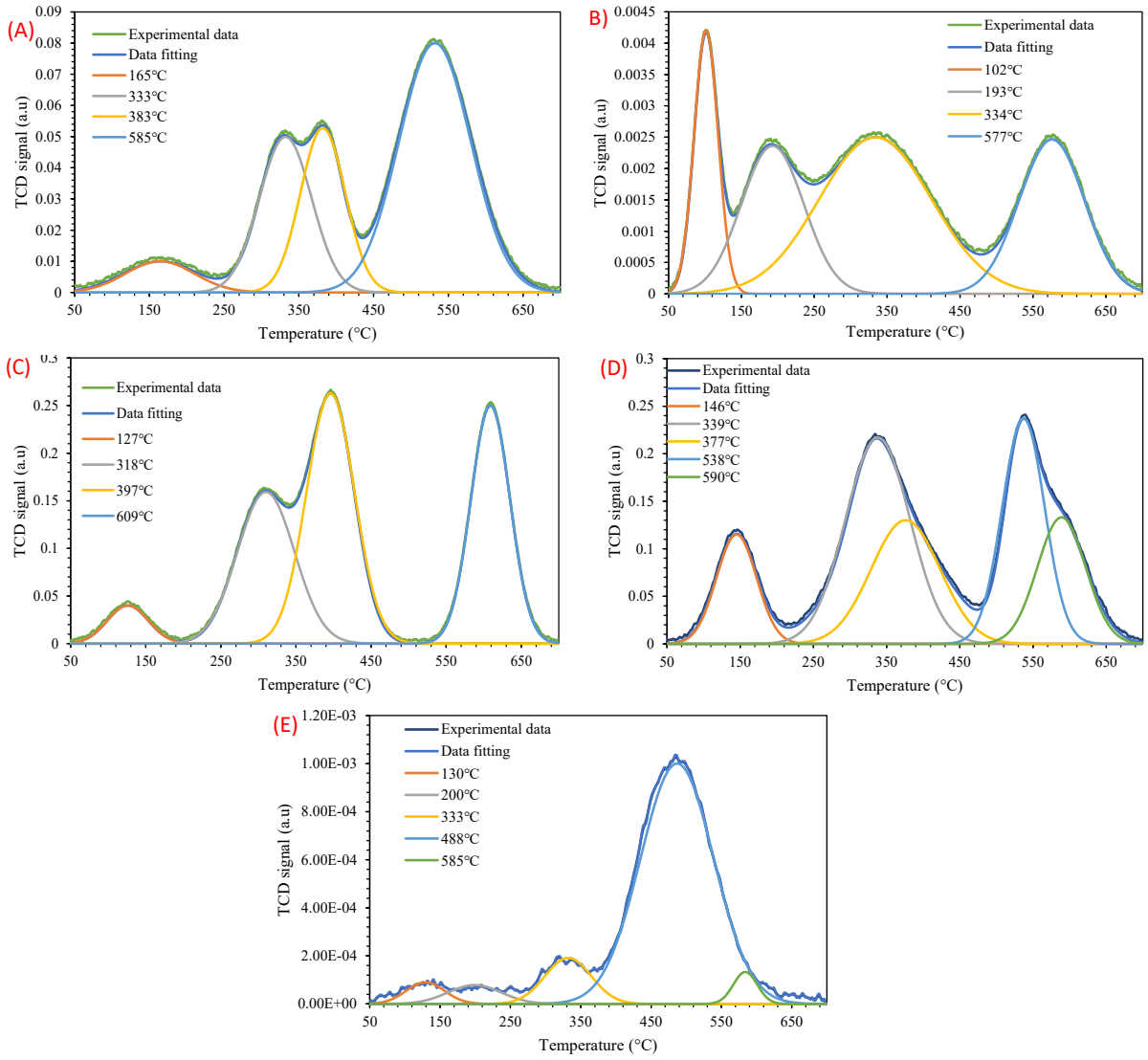


Fig. 3. TPD-NH_3 analysis for (A) Fe_3O_4, (B) $Si@Fe_3O_4$, (C) $NiSi@Fe_3O_4$, (D) $MoNiSi@Fe_3O_4$ and (E) $CoNiSi@Fe_3O_4$

Table 3. Acidic and magnetic properties.

Catalyst	**TPD-NH_3**		**VSM**	
	Weak + medium acid (T= 90-350°C) (µmol/g)[a]	**Strong acid (T= > 350-600°C) (µmol/g)[a]**	**MS (emu/g)[b]**	**Hc (Or)[b]**
Fe_3O_4	44.37	1125.9	115.29	12.64
$Si@Fe_3O_4$	124.83	572.04	52.01	10.17
$NiSi@Fe_3O_4$	311.13	1082.34	28.76	16.09
$CoNiSi@Fe_3O_4$	4638.96	38.34	36.86	30.18
$MoNiSi@Fe_3O_4$	316.71	270.9	34.69	14.14

[a] NH_3-TPD. [b]Vibrating sample magnetometer.

Magnetic properties of all catalysts were measured by VSM at room temperature (**Fig. 4** and **Table 3**). As expected, Fe_3O_4 exhibited a strong saturation magnetisation (Ms). All modification protocols lowered the Ms value, which decreased in the order Fe_3O_4 > $Si@Fe_3O_4$ > $CoNiSi@Fe_3O_4$ ~ $MoNiSi@Fe_3O_4$ > $NiSi@Fe_3O_4$. decrease in coercivity, by means additional of metal species into Fe_3O_4 affects both the catalyst's surface and the interaction between spins. Overall, all catalysts have maintained their ferromagnetic qualities at room temperature.

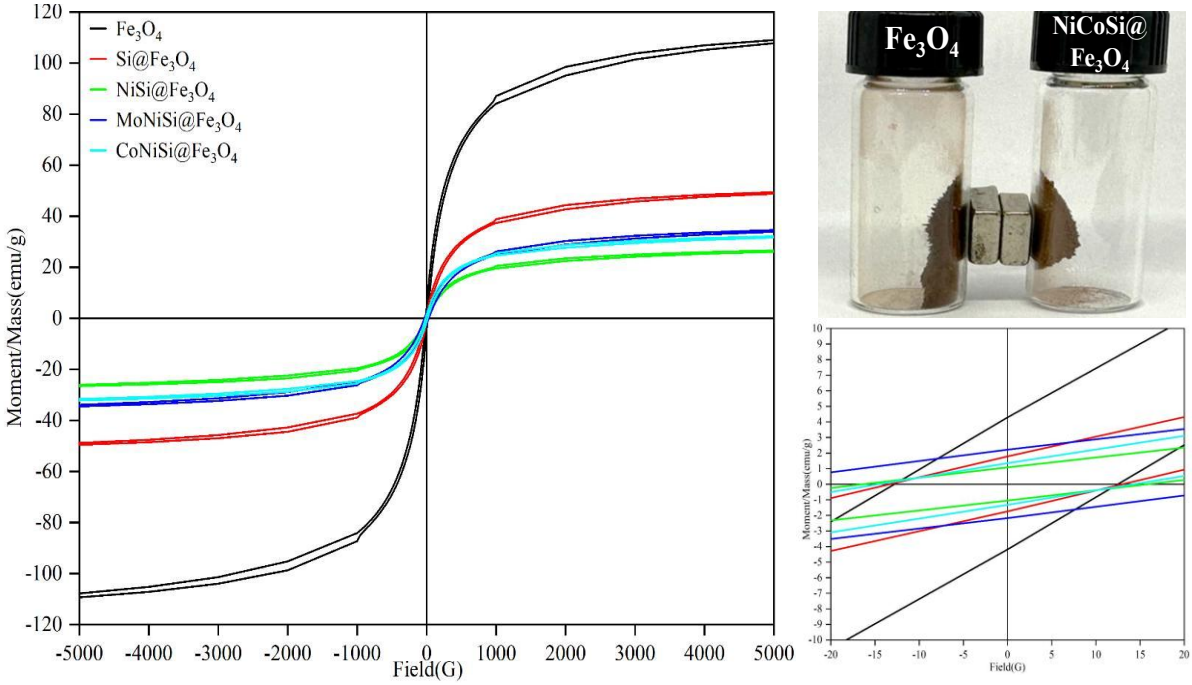


Fig. 4. VSM analysis of Fe_3O_4 and core-shell catalysts

Catalytic DO of palm kernal oil

Theoretically, for liquid phase DO reaction occurred on external surface of catalyst, since the magnetic Fe_3O_4 located inside the Si for $Si@Fe_3O_4$, hence it is believed that it will not significantly affect DO reaction activity as the Fe_3O_4 uniformly covered by Si phase (see FESEM). Similar with $Si@Fe_3O_4$, Si considering poor acid sites, one may assume that this catalyst also will not be explored. Considering the key role of Ni, Co, and Mo in affecting DO activity, the present study focused on DO of PKO over $NiSi@Fe_3O_4$, $CoNiSi@Fe_3O_4$, and $MoNiSi@Fe_3O_4$ catalysts. The GCFID result is depicted in **Fig. 5a**, whereby the $NiSi@Fe_3O_4$ yielded a similar total hydrocarbon percentage to the $CoNiSi@Fe_3O_4$ (>75%), with the liquid product consisting of linear hydrocarbons (C_8–C_{20}). The result shows that both Ni and CoNi-promoted $Si@Fe_3O_4$ supports can assist in the formation of rich hydrocarbon liquid products. Nevertheless, the trends of hydrocarbons produced from Ni and CoNi-catalysed DO vary, whereby DO product undecane (n-C_{11}) and pentadecane (n-C_{15}) dominated by $CoNiSi@Fe_3O_4$, while $NiSi@Fe_3O_4$ favours the formation of n-C_{11} and tridecane (n-C_{13}) (**Fig. 5b**). It has been agreed that all liquid products were created from the triglycerides in PKO. Since, the main components of triglycerides in PKO are C_{12}, C_{14}, C_{16} and C_{18} fatty acids. Thus, formation of n-C_{11}, n-C_{13}, n-C_{15} and n-C_{17} hydrocarbon have one carbon atom less, indicates that decarbonylation and decarboxylation (deCOx) removed

most of the oxygen in the fatty acids [6]. Parenthetically, total % of n-C_{11}, n-C_{13}, n-C_{15} and n-C_{17} were found higher in catalysed CoNiSi@Fe_3O_4 than NiSi@Fe_3O_4. Because Co has higher electrophilicity (Lewis acid sites, see **Table 3**) than Ni site, the electronegative oxygen atoms of C = O and C–O bonds more preferentially absorbed on the Co site than on Ni site [33]. This can account for the fact that the DO via deCOx pathway dominates on NiCo surfaces. The highest proportion of light fraction (C9-10) was obtained by NiSi@Fe_3O_4, suggesting that this catalyst is effective cracking reactions. Indeed, Co-promotion successfully curbs cracking activity of Ni [29]. In addition, C_{12} and C_{16} production on NiSi@Fe_3O_4 was more remarkable than other catalysts, suggesting it was more favourable to catalyse the HDO pathway and so the carbon loss was reduced [34]. This was mainly attributed to the large density of high-strength strong acid (Bronsted acid) in Ni, leading to the increase of competitive adsorption of strongly carbonaceous species on the catalyst surface, which facilitated the occurrence of secondary reactions. Minimal activity was observed over MoNiSi@Fe_3O_4 with unselective hydrocarbon products. Although a former study reported that Mo sites favoured decarbonylation pathway [33], however low acidic properties of MoNiSi@Fe_3O_4 obviously limit C-O bond cleavage activity. Based on bio-jet selectivity (C_{10}-C_{16}) (**Fig. 5a**), NiSi@Fe_3O_4 and CoNiSi@Fe_3O_4 clearly led to an increase in bio-jet selectivity than MoNiSi@Fe_3O_4. It is worth pointing out that all catalysed DO reaction are also strongly dependent of the catalyst's textural properties; evidently, CoNiSi@Fe_3O_4 with a surface area 66 m^2/g pore exhibited higher hydrocarbon yield and bio-jet selectivity.

A closer look at the deoxygenated liquid product analysed by GCMS shows that the n-paraffins (saturated hydrocarbons) are remarkably higher than the olefins (**Fig. 5c**). The formation of n-paraffins with one carbon atom shorter than the fatty acid in the feedstock is consistent with the results for GCFID shown in **Fig. 5b**. The C_{11} and C_{15} n-paraffins were found at 44%, which is higher than olefins (3%) and strongly agrees that decarboxylation pathways are more dominant than decarbonylation. This high % of light fractions n-(C_9-C_{10}) and n-(C_{19}-C_{22}) in NiSi@Fe_3O_4 catalysed product is evidence that Ni-rich catalyst favours cracking and polymerization reactions. As discussed above, a large density of high strength strong acid sites will increase the chances of the occurrence of undesirable secondary reactions. When compared with CoNiSi@Fe_3O_4 and NiSi@Fe_3O_4 acidity-DO and acidity-cracking activity achievement, the DO activity is found to be strongly dependent on the existence of a total weak-medium acid (Lewis's acid) catalyst, while cracking occurs specifically in relation to the strong acidic (Bronsted acid) site distribution. Similar with GCFID, the HDO (C_{12}, C_{16}) product dominated by NiSi@Fe_3O_4 catalysed reaction (24%). **Fig. 5d and Fig. S1** shows the formation of carboxylic acid, ketone, aldehyde, alcohol, and ester, which were produced from DO of PKO over core-shell catalysts. Noted, carboxylic acid and ketones were found to be larger. Results suggest that fatty acids are the primary products of triglyceride cracking and ketones are secondary products produced from direct ketonization of the fatty acids [35]. Noted, for all reactions, carboxylic acid decreases in the order NiSi@Fe_3O_4 < CoNiSi@Fe_3O_4 < MoNiSi@Fe_3O_4, based on TPD-NH_3 results (**Table 3**) implying that high acidic catalysts can selectively reduce carboxylic acids and readily converted. The numbers of ketone species were also the highest in both MoNiSi@Fe_3O_4 (~30%) and NiSi@Fe_3O_4 (25%), while CoNiSi@Fe_3O_4 showed

the least ketones species (~15%). Enriched 12-tricosanone by MoNiSi@Fe_3O_4 and NiSi@Fe_3O_4 catalysed reactions could be proof of the fact that weaker adsorption (due to low acidic sites) and stronger adsorption (due to Bronsted acid rich acid sites) boost the competitive adsorption of highly carbonaceous species on the catalyst surface, thereby initiating direct ketonisation $C_{12:0}$ fatty acid forming 12-tricosanone [36]. Indeed, lower ketones species recorded on CoNiSi@Fe_3O_4-catalyzed DO suggest rich Lewis acid sites can provide guidance on controlling the ketonisation process. In conclusion, higher acid strengths and less acidic sites will increase ketonisation activity and decrease product stability [37]. Overall, CoNiSi@Fe_3O_4 is the ideal catalyst for DO of PKO forming rich bio-jet fuel recombined with stable liquid product. A closer look on GCMS result of liquid product obtained from CoNiSi@Fe_3O_4 catalysed DO (**Fig. S1**), particularly carboxylic acid obtained, which was majorly comprised of dodecanoic acid ($C_{12:0}$) and tetradecanoic acid ($C_{14:0}$) with a total % of 16%, followed by a trace amount of octanoic acid ($C_{8:0}$), n-decanoic acid ($C_{10:0}$), and 9-octadecenoic acid ($C_{18:0}$) with a total of about 0.6%. Only traces number of aldehydes (tridecanedial; $C_{13}H_{24}O_2$), alcohol (phenol) and cyclic species (cyclopentane, cyclohexene, cyclopropane) are detected. In the case of ketones, majority ketones product composed of 8-octadecanone ($C_{18}H_{36}O$) (5%) and 12-tricosanone ($C_{23}H_{46}O$) (8%), respectively.

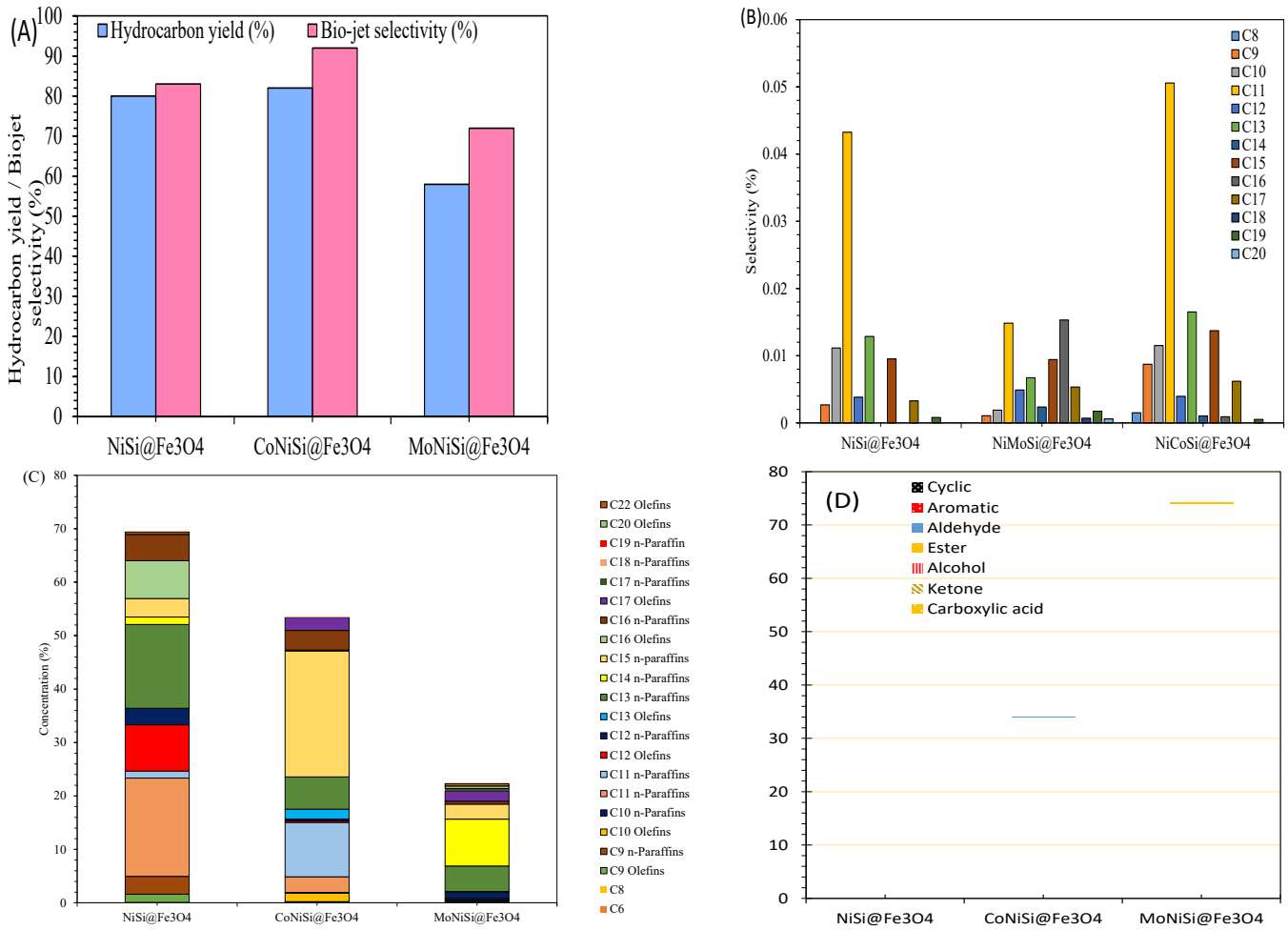


Fig. 5. (A) Hydrocarbon yield and bio-jet selectivity, (B) Carbon distribution product (C) Hydrocarbon product distribution and (D) By-product DO PKO product distribution in deoxygenated liquid product

produced by catalysed 5wt.% NiSi@Fe_3O_4, CoNiSi@Fe_3O_4 and MoNiSi@Fe_3O_4 catalyst at 350 ℃ within 3 h reaction time under N_2 flow reaction condition.

Fig. S2 shows the gas distribution of DO obtain using CoNiSi@Fe_3O_4. It is worth noting that CO_2 predominated, followed by CO and H_2. This result confirms that the PKO DO proceeds mainly through the decarboxylation reaction. It is worth noting that due to the detection of CO, CO_2, and H_2 by GCTCD and the production of decarbonylation by-product (H_2O), it can be speculated that the reactions such as water gas shift (WGS) and methanation could also take place [38]. Effective WGS and methanation processes over CoNiSi@Fe_3O_4 are supported by thermodynamic calculations, whereby this reaction path is highly likely to occur at 350 °C (see **Fig. 6**) [39,40]. Nevertheless, CH_4 gas remains absent because its concentration is below the detection limit. Theoretically, H_2 can also be produced via the cracking reaction. Since the DO carried out an H_2-free reaction condition, low H_2 pressure will not be able to push the WGS toward increasing CO formation [41]. Noteworthy to mention. The CO is known to preferentially adsorb on surface and simultaneously deactivate the surfaces. Since CO_2 predominates in gas products, the influence of CO would be lessened in our study.

Proposed reaction mechanism for CoNiSi@Fe_3O_4

By considering to the product distribution from GCMS results and Zulkifli's studies in DO of triolein derived triglycerides (TAG), mechanism of DO PKO can be proposed [42], first, the TAG in PKO underwent C-C bond scission via the β-elimination of hydrogen to form 1 unit of fatty acid such as dodecanoic acid ($C_{12}H_{24}O_2$), tetradecanoic acid ($C_{14}H_{30}O_2$), hexadecenoic acid ($C_{16}H_{34}O_2$) and 9-octadecenoic acid ($C_{18}H_{38}O_2$) (Eq. A) (**Fig. 6**). The resulting fatty acid can be further cracked by removing of the terminal carbons (CH_2-) leading to the formation of saturated acids (e.g., caprylic acid, nonanoic acid, decanoic acid) (Eq. B). Dodecanoic acid and hexadecenoic acid were initially decarboxylated forming saturated undecane ($C_{11}H_{24}$), tridecane ($C_{13}H_{38}$), pentadecane ($C_{15}H_{32}$) and heptadecane ($C_{17}H_{36}$) as major products simultaneously releasing CO_2 (Eq. C). Besides, the decarbonylation (-CO, H_2O) of those fatty acids occurs simultaneously to produce the unsaturated hydrocarbons 1-undecene ($C_{11}H_{22}$), 1-tridecene ($C_{13}H_{36}$), 1-pentadecene ($C_{15}H_{30}$) and 1-heptadecene (C17H34), simultaneously forming carbon monoxide (-CO) and water (-H_2O) (Eq. D). Indeed, the formation of undecane, tridecane, pentadecane and heptadecane (DO alkanes species) can be achieved through hydrogenation under a minimum H_2 atmosphere (Eq. E). The presence of the acid catalyst from CoNiSi@Fe_3O_4 catalyst facilitates the transfer of H* which then hydrogenates DO alkene species to produce the corresponding DO alkanes. The hydrogenation was probably assisted by in-situ hydrogen produced from the water gas shift reaction (WGS) ($CO+H_2O \rightarrow CO_2+H_2$) (Eq F) and cracking reaction (Eq. B) [43]. This phenomenon is in accordance with a previous study, which shows that the WGS reaction occurs naturally during decarbonylation, thereby releasing CO_2 and H_2 [44]. Indeed, the formation of 1-undecene isomers was observed as part of the DO mechanism via H_2-transfer [42] (Eq. G). Then those isomers further crack, forming

short-chain hydrocarbons (hexane, octane, nonane decane) that are recombined with the cyclization of short-chain hydrocarbons such as propane, pentane, and hexane, forming cyclic species (Eq. H). Ravindran et al confirm that those cracking activities occur on terminal carbon (-CH_2) of saturated hydrocarbon H_2 [13]. Indeed, some short-chain hydrocarbons (such as nonane and decane) underwent dehydrogenation, forming 1-nonene and 1-decene (Eq. I)[45]. These unsaturated hydrocarbons can be transformed back to saturated hydrocarbons via hydrogenation reactions. Noted, GCMS also detected the formation of C_{12} and C_{16} alkanes, which gave an indication that dehydrodeoxygenation of dodecanoic acid and hexadecenoic acid occurred as a by-product of H_2O (Eq. J). Other detected side products were the ketones, which corresponds well with our assumption that self-ketonisation of pentadecanoic acid occurred due to the in-situ ketonisation resulting in the long-chain hydrocarbons 8-octadecanone ($C_{18}H_{36}O$) and 12-tricosanone ($C_{23}H_{46}O$) (Eq. K). The gas composition present in this study consisted of H_2, CO, and CO_2 in addition to saturated and unsaturated hydrocarbons, mostly those in the bio-jet fuel range. As discussed above, the H_2 was probably produced via cracking (Eqs. B, H) and WGS reactions (Eq. F). Since the reaction consisted of CO and H_2, it can be speculated that methane gas might also be produced during

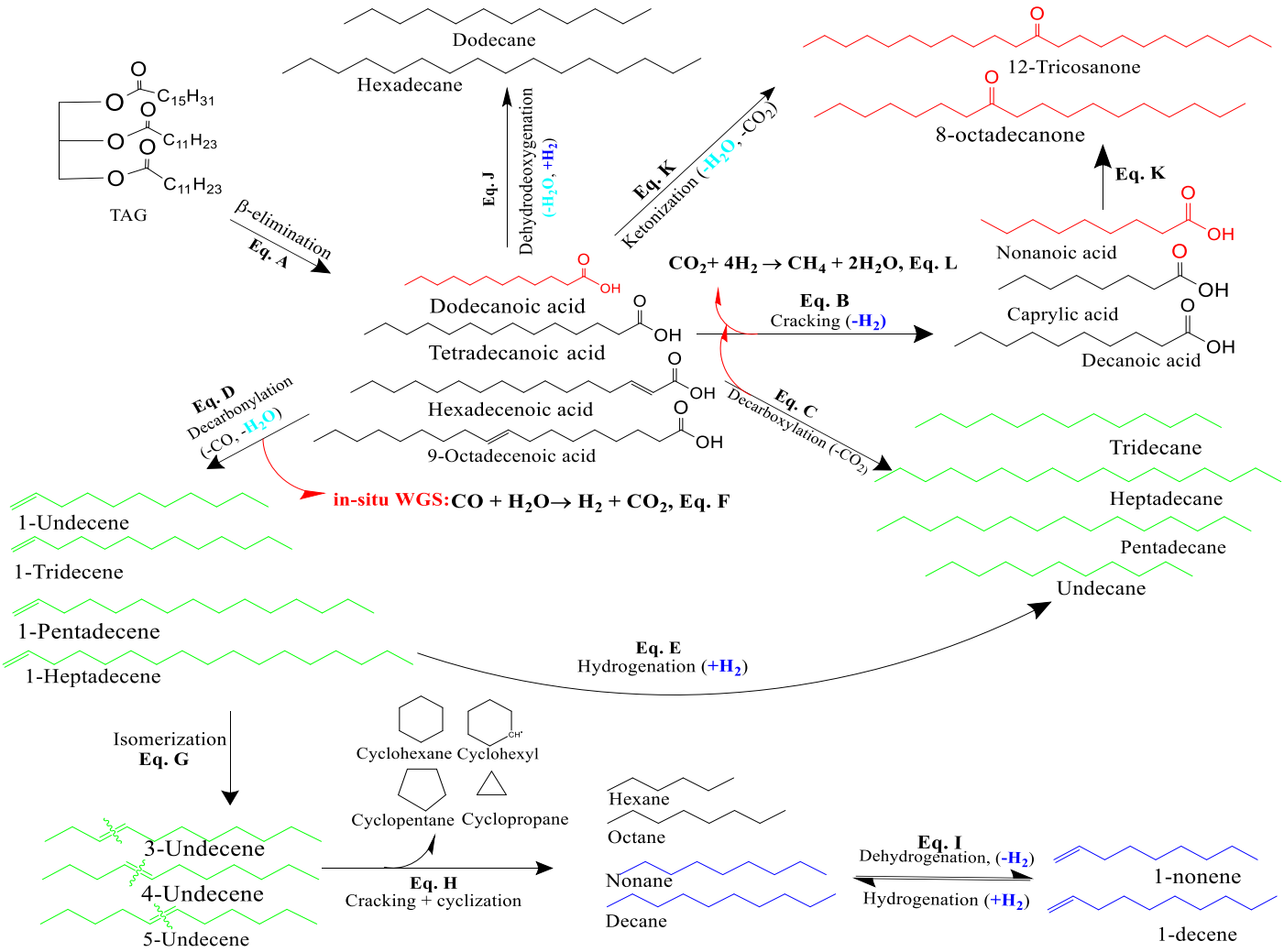


Fig. 6. Mechanism of DO PKO over CoNiSi@Fe_3O_4 catalystthe methanation reaction (Eq. L) and generate H_2O as a by-product.

Noted, the methane has been detected in our previous DO study, but the amount is in traces [46]. Overall, based on the above findings, it is likely that the high activity for conversion of PKO under an inert atmosphere yields significant formation of unsaturated compounds, which in turn may cause catalyst deactivation. Therefore, in the next section, we focus on the investigation of the deactivation of the CoNiSi@Fe_3O_4 catalyst during DO of PKO.

Deactivation of CoNiSi@Fe_3O_4

Here we evaluate of catalyst deactivation within a chemical process. We employ the second-order power-law deactivation model to analyse the relative rate, which signifies the change in alkane yield over time compared to the initial yield at t = 0 (as depicted in **Fig. 7i a-c**). Various power-law models were explored, with the second-order variation yielding the most precise fit. Previous literature suggests that first-order models are apt for situations with minimal pore diffusion resistance [47], whereas higher-order models find more relevance in cases with substantial pore diffusion resistance, commonly referred to as fouling. The findings strongly indicate that in this context, the principal mechanism of catalyst deactivation is fouling rather than active site poisoning. Moreover, the deactivation rate constant (k_{deac}) demonstrated a rising pattern in the sequence of 330℃ (1.01×10^{-2} h^{-1}) < 350℃ (2.72×10^{-1} h^{-1}) < 300℃ (1.01908 h^{-1}). Following a 500-min reaction period, the quantification of coke on the CoNiSi@Fe_3O_4 catalyst was conducted using TPO. The coke content similarly followed an ascending order: 330℃ (972.5 µmol g^{cat-1}) < 300℃ (1137.2 µmol g^{cat-1}) < 350℃ (2999.7 µmol g^{cat-1}) (**Table 5**), suggesting that the primary reason for the catalyst's deactivation was predominantly attributed to coke accumulation on the catalyst. Considering the total coke deposition and the formation of heavy products (4%, C_{22}) in **Fig.5**, it is reasonable to surmise that coke species were generated through subsequent processes such as polymerization, cyclization, and hydrogen transfer from the heavier products. To gain deeper insights into the deactivation mechanism, an analysis of the remaining porosity of the catalyst collected after 500 min of PKO conversion was conducted. The results unveiled a significant reduction in pore volume, decreasing from 9 cm^3 g^{-1} to 0.01 cm^3 g^{-1} (**Table 5).** This outcome signifies that even nitrogen (N_2) molecules encountered difficulties in accessing the pores of the deactivated catalyst. This observation corroborates the earlier deduction that fouling stands as the primary deactivation mechanism, aligning consistently with the previously discussed second-order power-law deactivation kinetics. An essential facet of catalysis science entails the establishment and clarification of the connections between a catalyst's structure and its functionality. This is accomplished by correlating the material properties of catalysts with their specific catalytic behaviours. To achieve this with precision, it is imperative to meticulously gauge reaction kinetics under conditions that align with the chosen characterization method. When dealing with solid catalysts analysed through ex-situ methods, obtaining a precise assessment of the initial catalytic rate on an unaltered surface is indispensable.

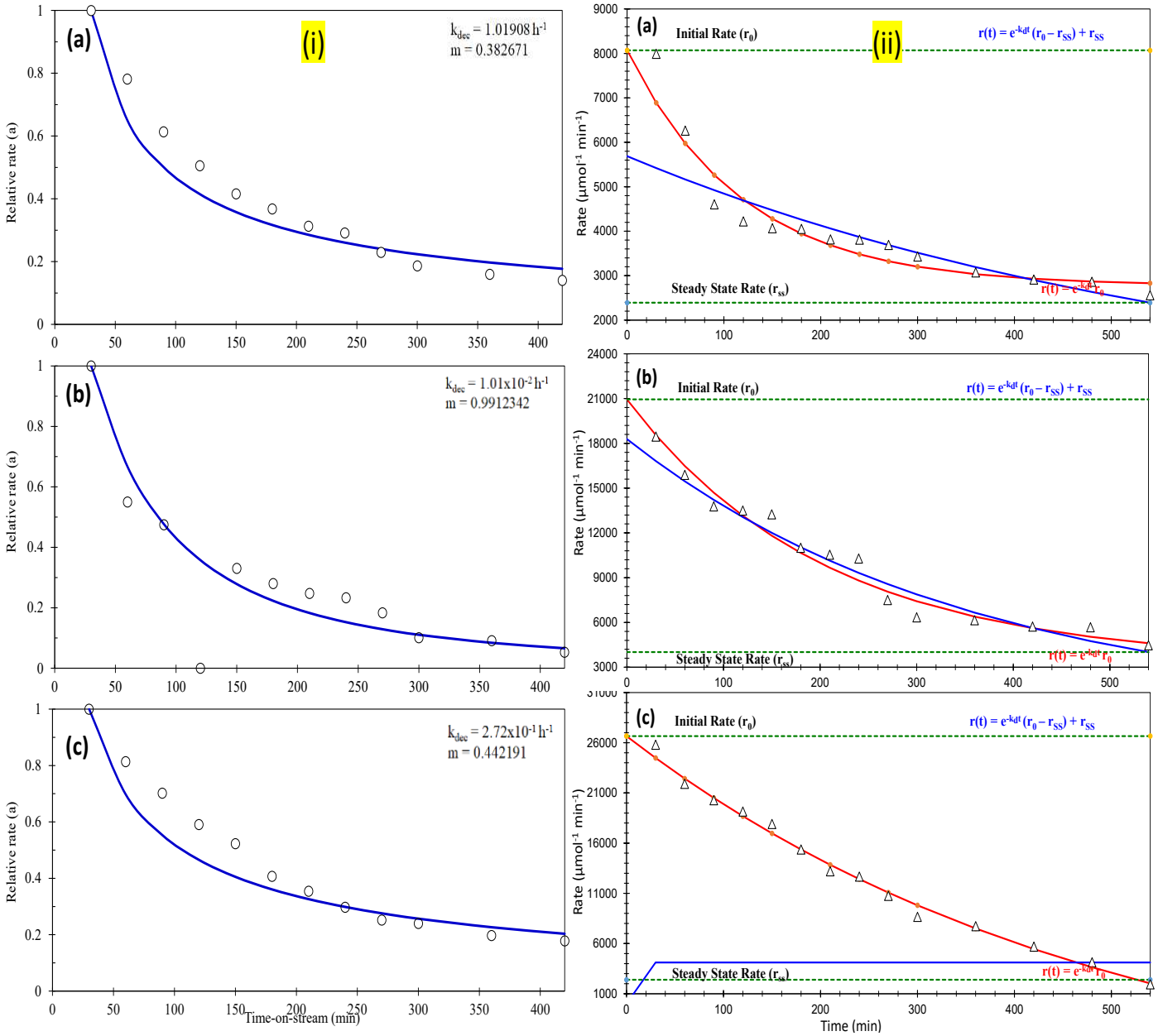


Fig. 7(i a–c) illustrates the second-order power-law deactivation fitting based on the relative rate, while Fig. 7(ii a–c) presents both the non-zero rate asymptote and zero-rate asymptote. The results correspond to reaction temperatures of (a) 300 °C, (b) 330 °C, and (c) 350 °C for the deoxygenation (DO) of PKO over 5 wt.% CoNiSi@Fe_3O_4 under an N_2 flow. The data are expressed as a function of time-on-stream during the DO process. The relative rate is defined as the ratio of hydrocarbon yield at time (t) to the initial hydrocarbon yield at (t = 0).

In catalysis research, examining both the non-zero rate asymptote and the zero-rate asymptote is of considerable importance. This approach enhances the understanding of catalyst deactivation behavior, suggesting that under prolonged continuous operation, a catalyst may progressively approach a zero reaction rate. Conversely, the first-order deactivation model with a non-zero rate asymptote assumes that the catalyst ultimately reaches a finite steady-state rate over extended time. As shown in Table 4 and Fig. 7(ii a–c), the steady-state rate ((r_{ss})) follows the order: −25242.5 µmol g^{-1} min^{-1} at 350 °C < −5615.0 µmol g^{-1} min^{-1} at

300 °C < −480.4 μmol g^{-1} min^{-1} at 330 °C. In contrast, the initial rate ((r_0)) exhibits the trend: 50840.5 μmol g^{-1} min^{-1} at 330 °C > 40974.7 μmol g^{-1} min^{-1} at 350 °C > 19267.5 μmol g^{-1} min^{-1} at 300 °C. These results indicate that, at prolonged reaction times, the system operating at 330 °C demonstrates the highest catalytic activity among the studied temperatures.

Table 4 presents the deactivation parameters for both the non-zero rate asymptote and the zero-rate asymptote of the CoNiSi@Fe_3O_4 catalyst, obtained by fitting the data through minimization of the sum of squared deviations using the SOLVER add-in.

Rate of Asymptote	**Temperature / °C**		
	300	**330**	**350**
Non-zero rate asymptote			
r_0 [μmol/g.min]	19267.5	50840.5	40974.7
kd[1/min]	3.4×10^{-3}	6.3×10^{-3}	1.9×10^{-3}
rss [μmol/g.min]	-5615.0	-480.4	-25242.5
Zero rate asymptote			
r_0 [μmol/g.min]	19252.9	52221.3	48989.9
kd[1/min]	3.4×10^{-3}	$6.6E\times10^{-3}$	$5.3E\times10^{-3}$
rss [μmol/g.min]	-5624.114267	0.004224135	0.004224135

Coking of CoNiSi@Fe_3O_4

The spent catalysts derived after the long-term time-on-stream experiments at different temperatures were investigated using TPO, UV Raman, NH_3-TPD, and BET in order to derive information regarding their loss of stability on both chemical and textural properties. Cocaine analysis and quantification are achieved by TPO analysis. **Fig. 8** shows the TPO oxidation peaks for all spent catalysts, and the results showed typical carbon-related bands at low temperatures; (i) ca: 200-400°C corresponds to C_α; atomic carbon adsorbed on the metal surface, (ii) ca: 200-500°C corresponds to C_β; polymeric amorphous films), (iii) ca: 500-550°C are ascribed C_c graphitic platelets or films and (iv) ca: 300-1000°C belong to C_v; filamentous coke [48]. Indeed, the major TPO peak showed the existence of both amorphous and graphitic carbon phases. The amorphous carbon phase is related to oxidation relative to the strongly adsorbed O-containing reactant or product on acid sites, while graphitic carbon is associated with deposits originated from polycyclic aromatic hydrocarbons (PAHs)[49,50]. Notably, the most reactive and amorphous carbonaceous molecules adsorbed on metal sites are C_α and C_β at lower temperatures, and at higher temperatures, they will change into stable carbon (C_v), which is progressively graphitized (C_c). Indeed, the TPO result evinced that the degree of graphitization increased with increments in DO temperature [51]. The quantified amount of carbon is 1137, 972 and 2999 μmol g^{cat-1} on Used-300, Used-330 and Used-350, respectively (**Table 5**).

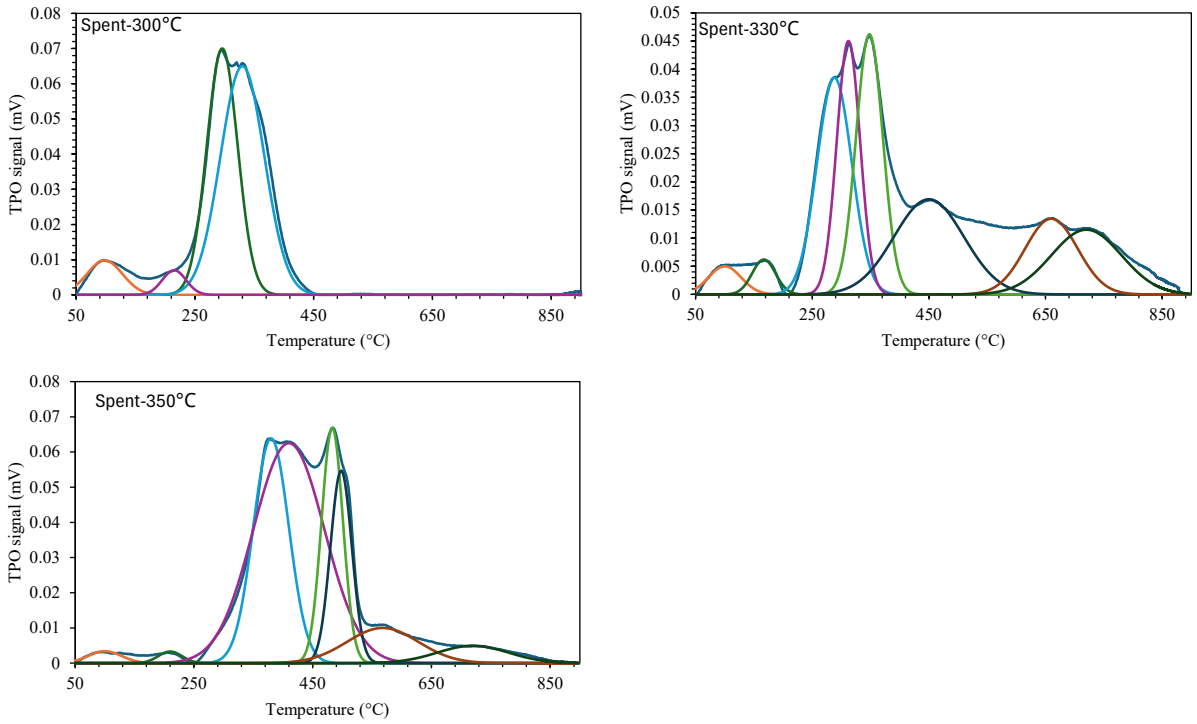


Fig. 8. TPO profile for used CoNiSi@Fe_3O_4 catalyst at DO reaction temperature 300, 330 and 350°C.

In fact, the low carbon content at 330 ºC (determined by TPO analysis) strongly implies that this is the optimal temperature for DO. **Fig. 9** shows in-situ Raman analysis for CoNiSi@Fe_3O_4 catalyst at 330 ºC within 0-270 min. The CoNiSi@Fe_3O_4 had two characteristic graphitic peaks at: ~1300 cm^{-1} and ~1600 cm^{-1}, which correspond to the D and G bands, respectively. A previous study found that the D peak is caused by the breathing modes of sp2 atoms in rings, whereas the G peak is caused by the bond stretching of all pairs of sp2 atoms in rings and chains [51]. According to Adegbenjo et al., the reduced Raman peak in the carbon catalyst is evidence of the extensive loss of crystallinity in the catalyst and the presence of an amorphous carbon phase [52]. In summary, the low intensity of the D and G bands in the present study is due to the amorphization of graphitic carbon. Notably, carbon deposited began at the onset time of 30 min (150 ºC) and increased with DO response time, as indicated by the trend increment of D and G bands acquired by the in-situ Raman examination. This result clearly indicates that longer DO times favour sp_2 disorder on the CoNiSi@Fe_3O_4 catalyst while also promoting a high degree of crystallinity in graphitic carbon. Ultimately, the catalyst's deactivation was sparked by graphitic carbon, which obscured the active sites and might have contributed to the catalyst's reduced DO performance. Noteworthy, over the course of the 270-min reaction, the G bands at 1493 cm^{-1} to 1521 cm^{-1}noticeably shifted to a higher frequency of 1610 cm^{-1} to 1636 cm^{-1}, which is associated with thermal stress at a longer DO period. He et al. suggested that this G band shifting is due to the deactivation by long-chain paraffin species (*n*-(C_{16}-C_{22})), which is possibly related to conjugated olefinic species, or PAHs (see **Fig. 5d, Fig. 6**)[51]. Generally, those species will intrinsically increase the formation of deep-dehydrogenation reaction forming coke. Zhang and his colleagues come to a similar result and also confirm that the generation of coke and catalyst acid sites is positively correlated [53]. A weak Raman band at 1200

$cm^{-1}$to 1600 cm^{-1} was also observed; this band appears only in very poorly organised carbonaceous compounds, but its identification is still the subject of controversy [28]. Nevertheless, this band remained weak throughout the DO reaction time, confirming a high graphitization degree in the resultant coke.

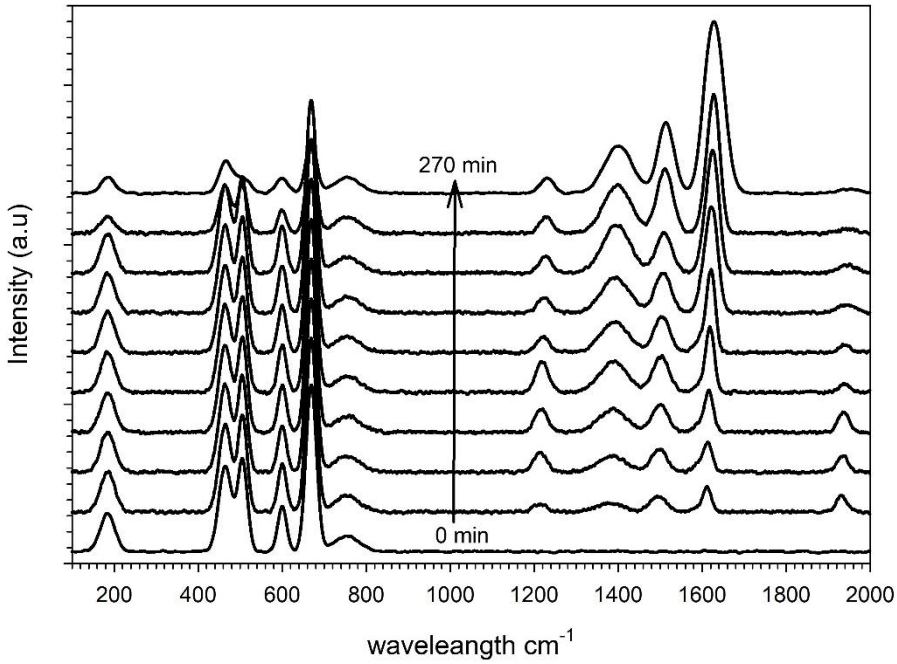


Fig. 8. In-situ Raman spectra of CoNiSi@Fe_3O_4 as a function of reaction time at 330 °C during PKO DO under flowing N_2.

BET measurements were carried out to investigate the textural modification after the coke deposition. As shown in **Fig. S3**, the nitrogen adsorption and desorption isotherms of the spent catalysts remain type IV and are almost the same as those of the fresh catalyst, suggesting the co-existence of micropores and mesopores. **Table 5** showed that there is reduction in the specific surface area and pore properties of Used-catalyst as compared to the fresh CoNiSi@Fe_3O_4. It is interesting to note that a striking pore volume reduction on Used-350 compared to other used catalysts strongly demonstrated that high reaction temperatures favour the creation of a thicker carbon layer inside catalyst particles. Barron's finding also agreed that the thickness of the carbon layer increased with reaction temperature [54]. As suggested by Songbo's study, most of the graphitic coke deposited has a flat epitaxial and layered structure, and raising the DO temperature apparently will increase the coke thickness at a given flat epitaxial position while at the same time causing metal sintering, thereby resulting in a loss of active surface area [51]. Overall, higher DO reaction temperatures provoked coke formation and negatively affected the textural properties of the catalyst.

Fig. 10a and Table 3 compares the total acidity of fresh and all used catalysts, revealing the acidity strength of fresh CoNiSi@Fe_3O_4 increases after reaction. Majority of used catalyst exhibited strong acid (Bronsted acid) sites, and the acid strength increased with DO temperature. As reported elsewhere, acidity is the

parameter that directly affects the chemisorption of reactants, and the chemisorption strength of the substance is related to the amount of acid on the catalyst [55]. Combining the results in Section 3.2, the formation of strong acid sites on used catalysts is the main reason for boosting the competitive chemisorption of highly carbonaceous species on the catalyst surface. By definition, an increment of strong acid strength will result in significant coke formation and mask active sites or block pores that contain active sites. Noteworthy, the total number of acid sites in used catalysts was found to be lower than in fresh catalysts, and their surface acidity decreased in the order of Used-330 > Used-350 > Used-300. Reduction of acidity after DO coincides with the formation of coke which deposited on the catalyst active sites. Indeed, high reaction temperatures do in fact lead to the formation of highly dense carbon deposits, nevertheless, the acid amount on Used-350 remains higher than that of Used-300. Based on this finding, it can be concluded that coke content does not influence acidity site density. According to a few sources [48,56], coke deposition occurs in catalytic processes that deal with hydrocarbon and oxygenate feedstocks and follows a few steps. As shown in **Figs. 10bi–iii**, there are three stages involved: (i) strong chemisorption as monolayer forming carbide group (MC) (M: metal, C: carbon) hindering access to active sites; (ii) total covering (encapsulation) of the active site making it inaccessible to the reactants (such as $C_nH_mO_k$ oxygenates followed by (iii) plugging of micropores and/or mesopores of the catalyst, which in this case directly blocks access to active sites in inner pores. In fact, coke growth will accelerate with an increase in reaction temperature, and this fact is in agreement with the dramatic reduction in pore volume on Used-350 (see **Table 5**) caused by the high number of carbonaceous species.

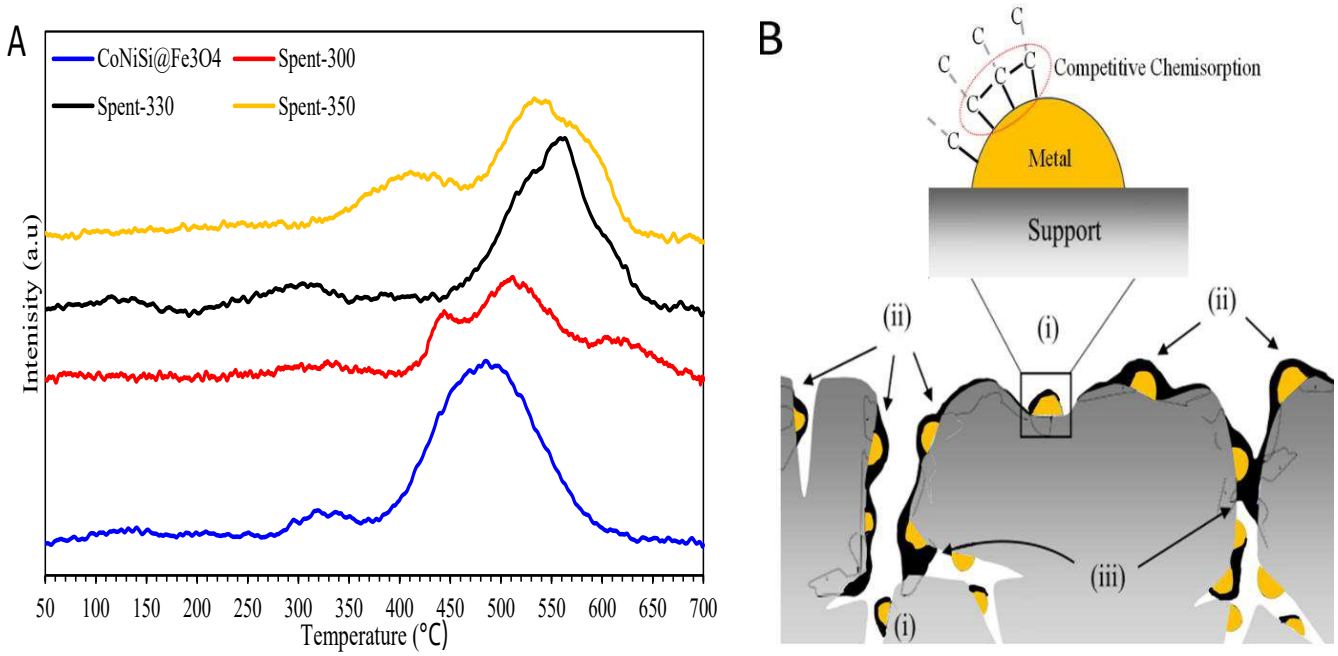


Fig. 10. (a) Acidity profile for fresh and used CoNiSi@Fe_3O_4 catalyst at DO reaction temperature 300, 330 and 350°C and (b) deactivation pathways by coke deposition on a supported metal catalyst: (i) carbon chemisorption hindering the access to reactants; (ii) metal particle encapsulation; (iii) pore plugging.

Table 5. Physicochemical properties of as-prepared and post-reaction CoNiSi@Fe_3O_4.

Catalyst[a]	BET[b] / $m^2 \cdot g^{-1}$	V_p[b] / $cm^3 \cdot g^{-1}$	Pore size[c] / nm	Acid loading[d] / mmol g^{-1}	Total carbon[e] / mmol.g^{cat-1}
As-prepared	66	9	0.22	4.68	-
300	37	0.1	8.8	2.44	1.14
330	5	0.0	14.7	4.11	0.97
350	6	0.0	8.4	3.75	3.00

[a]Post-reaction after 3 h PKO DO at specified temperature. [b]BET. [c]BET method. [d]TPD-NH_3. [e]TPO.

Conclusions

The synthesised NiSi@Fe_3O_4, MoNiSi@Fe_3O_4, and CoNiSi@Fe_3O_4 catalysts were core-shell catalysts with magnetic responsiveness for easy separation. The CoNiSi@Fe_3O_4 catalyst presented higher DO activity via the deCOx reaction than NiSi@Fe_3O_4, and MoNiSi@Fe_3O_4 showed the least DO activity. Cobalt modification plays an important role in the development of enriched weak + medium acid (Lewis acid) sites, which are responsible for effective adsorbed C=O and C-O bonded species on catalyst surfaces, thereby boosting the DO reaction via deCOx pathways leading to rich bio-jet fuel hydrocarbons. A larger number of strong acid (Bronsted acid) sites on NiSi@Fe_3O_4 boosts the competitive adsorption of highly carbonaceous species on the catalyst surface, which results in the occurrence of competitive reactions such as DO, cracking, HDO reactions, and ketonization, yielding a noticeable distribution of light (C_9), bio-jet (C_{10}–C_{16}), heavy hydrocarbon (C_{22}) fractions ($C_{9\text{-}22}$), and ketones species. Rich detection of CO_2 species and formation of DO alkanes confirm that the PKO DO over CoNiSi@Fe_3O_4 catalyst proceeds mainly through the decarboxylation reaction. Indeed, the deactivation kinetic study confirms that the deactivation happens by the coke formation and follow of second-order deactivation. In conclusion, we've determined that coking—which is mostly in the form of graphite—is the key factor in the deactivation of catalysts. The rate of growth of graphitic carbon from amorphous carbon increases in direct proportion to the rise in DO reaction temperature. Noted, coke content on the catalyst surface does not influence acid site density.

Acknowledgement

This research was financially supported by the Ministry of Higher Education, Malaysia, for niche area research under the Higher Institution Centre of Excellence (HICoE) program (JPT(BKPI)1000/016/018/28 Jld.3(2) & NANOCAT-2024E) and the financial support from GP-K023310.

Ethics, Consent to Participate, and Consent to Publish declarations: not applicable.

Funding Declaration

The authors gratefully acknowledge financial support from the Ministry of Higher Education, Malaysia, for niche area research under the Higher Institution Centre of Excellence (HICoE) program (JPT(BKPI)1000/016/018/28 Jld.3(2) & NANOCAT-2024E) and the financial support from GP-K023310.

References

[1] L. Paddison, J. Gretener, 'Sounding the alarm': World on track to breach a critical warming threshold in the next five years, Cnn (2023). https://edition.cnn.com/2023/05/17/world/global-warming-breach-wmo-climate-intl/index.html.

[2] G.R. Ciottone, M.E. Gebhart, Hurricanes, Cyclones, and Typhoons, Ciottone's Disaster Med. (2024) 598–600. https://doi.org/10.1016/b978-0-323-80932-0.00095-1.

[3] B. Tan, Parts of Malaysia at risk of disappearing due to global warming-induced sea level rise, 2023. https://www.malaymail.com/news/malaysia/2023/05/18/report-parts-of-malaysia-at-risk-of-disappearing-due-to-global-warming-induced-sea-level-rise/69811.

[4] T. Morgan, E. Santillan-Jimenez, A.E. Harman-Ware, Y. Ji, D. Grubb, M. Crocker, Catalytic deoxygenation of triglycerides to hydrocarbons over supported nickel catalysts, Chem. Eng. J. 189–190 (2012) 346–355. https://doi.org/10.1016/j.cej.2012.02.027.

[5] P. Priecel, L. Čapek, D. Kubička, F. Homola, P. Ryšánek, M. Pouzar, The role of alumina support in the deoxygenation of rapeseed oil over NiMo-alumina catalysts, Catal. Today 176 (2011) 409–412. https://doi.org/10.1016/j.cattod.2010.11.022.

[6] G. Abdulkareem-Alsultan, N. Asikin-Mijan, L.K. Obeas, R. Yunus, S.Z. Razali, A. Islam, Y. Hin Taufiq-Yap, In-situ operando and ex-situ study on light hydrocarbon-like-diesel and catalyst deactivation kinetic and mechanism study during deoxygenation of sludge oil, Chem. Eng. J. 429 (2022) 132206. https://doi.org/10.1016/j.cej.2021.132206.

[7] J.O. Shim, K.W. Jeon, W.J. Jang, H.S. Na, J.W. Cho, H.M. Kim, Y.L. Lee, D.W. Jeong, H.S. Roh, C.H. Ko, Facile production of biofuel via solvent-free deoxygenation of oleic acid using a CoMo catalyst, Appl. Catal. B Environ. 239 (2018) 644–653. https://doi.org/10.1016/j.apcatb.2018.08.057.

[8] P. Summa, K. Świrk Da Costa, Y. Wang, B. Samojeden, M. Rønning, C. Hu, M. Motak, P. Da Costa, Effect of cobalt promotion on hydrotalcite-derived nickel catalyst for CO2 methanation, Appl. Mater. Today 25 (2021) 1–41. https://doi.org/10.1016/j.apmt.2021.101211.

[9] F.P. Sousa, L.N. Silva, D.B. de Rezende, L.C.A. de Oliveira, V.M.D. Pasa, Simultaneous deoxygenation, cracking and isomerization of palm kernel oil and palm olein over beta zeolite to produce biogasoline, green diesel and biojet-fuel, Fuel 223 (2018) 149–156. https://doi.org/10.1016/j.fuel.2018.03.020.

[10] B. Peng, X. Yuan, C. Zhao, J.A. Lercher, Stabilizing catalytic pathways via redundancy: Selective reduction of microalgae oil to alkanes, J. Am. Chem. Soc. 134 (2012) 9400–9405. https://doi.org/10.1021/ja302436q.

[11] N.A. Abdul Razak, N.A. Mijan, Y.H. Taufiq-Yap, D. Derawi, Production of green diesel via hydrogen-

free and solventless deoxygenation reaction of waste cooking oil, J. Clean. Prod. 366 (2022) 132971. https://doi.org/10.1016/j.jclepro.2022.132971.

[12] Y. Zhao, H. Li, H. Li, NiCo@SiO2 core-shell catalyst with high activity and long lifetime for CO2 conversion through DRM reaction, Nano Energy 45 (2018) 101–108. https://doi.org/10.1016/j.nanoen.2017.12.023.

[13] M.X.Y. Ravindran, N. Asikin-Mijan, H.C. Ong, D. Derawi, M.R. Yusof, M.S. Mastuli, H. V. Lee, W.N.A.S. Wan Mahmood, M.S. Razali, G. Abdulkareem Al-Sultan, Y.H. Taufiq-Yap, Feasibility of advancing the production of bio-jet fuel via microwave reactor under low reaction temperature, J. Anal. Appl. Pyrolysis 168 (2022). https://doi.org/10.1016/j.jaap.2022.105772.

[14] J. Wu, Q. Sun, J. Lu, Synthesis of magnetic core-shell Fe3O4@SiO2@Mg(OH)2composite using waste bischofite and its catalytic performance for ozonation of antibiotics, J. Environ. Chem. Eng. 8 (2020) 104318. https://doi.org/10.1016/j.jece.2020.104318.

[15] A.S. Kamzin, H. Das, N. Wakiya, A.A. Valiullin, Magnetic Core/Shell Nanocomposites MgFe2O4/SiO2 for Biomedical Application: Synthesis and Properties, Phys. Solid State 60 (2018) 1752–1761. https://doi.org/10.1134/S1063783418090147.

[16] R. Nava, B. Pawelec, P. Castaño, M.C. Álvarez-Galván, C. V. Loricera, J.L.G. Fierro, Upgrading of bio-liquids on different mesoporous silica-supported CoMo catalysts, Appl. Catal. B Environ. 92 (2009) 154–167. https://doi.org/10.1016/j.apcatb.2009.07.014.

[17] J. Chen, Y. Yang, H. Shi, M. Li, Y. Chu, Z. Pan, X. Yu, Regulating product distribution in deoxygenation of methyl laurate on silica-supported Ni-Mo phosphides: Effect of Ni/Mo ratio, Fuel 129 (2014) 1–10. https://doi.org/10.1016/j.fuel.2014.03.049.

[18] M. Shahinuzzaman, Z. Yaakob, Y. Ahmed, Non-sulphide zeolite catalyst for bio-jet-fuel conversion, Renew. Sustain. Energy Rev. 77 (2017) 1375–1384. https://doi.org/10.1016/j.rser.2017.01.162.

[19] C. Gutiérrez-Antonio, F.I. Gómez-Castro, J.A. de Lira-Flores, S. Hernández, A review on the production processes of renewable jet fuel, Renew. Sustain. Energy Rev. 79 (2017) 709–729. https://doi.org/10.1016/j.rser.2017.05.108.

[20] E.S.K. Why, H.C. Ong, H.V. Lee, W.H. Chen, N. Asikin-Mijan, M. Varman, W.J. Loh, Single-step catalytic deoxygenation of palm feedstocks for the production of sustainable bio-jet fuel, Energy 239 (2022) 122017. https://doi.org/10.1016/j.energy.2021.122017.

[21] E.S.K. Why, H.C. Ong, H.V. Lee, W.H. Chen, N. Asikin-Mijan, M. Varman, Conversion of bio-jet fuel from palm kernel oil and its blending effect with jet A-1 fuel, Energy Convers. Manag. 243 (2021) 114311. https://doi.org/10.1016/j.enconman.2021.114311.

[22] Vegetable Fats and Oils, in: Fats Oils Handb., AOCS Press, 1998: pp. 174–344. https://doi.org/10.1016/b978-0-9818936-0-0.50009-3.

[23] K.M. Makhdum Munawar, K. Simarani, M.S. Mohamad Annuar, Bioconversion of mixed free fatty acids to poly-3-hydroxyalkanoates by Pseudomonas putida BET001 and modeling of its fermentation in shake flasks, Electron. J. Biotechnol. 19 (2016) 50–55. https://doi.org/10.1016/j.ejbt.2015.07.005.

[24] Microsoft, Define and solve a problem by using Solver. (Retrieved March 24, 2014), Https://Support.Office.Com/En-Us/Article/Define-and-Solve-a-Problem-by-Using-Solver-9ed03c9f-7caf-4 (2014). http://office.microsoft.com/en-us/excel-help/define-and-solve-a-problem-by-using-solver-HP010072691.aspx (accessed July 27, 2021).

[25] Z. An, H. Wang, C. Zhu, H. Cao, J. Xue, Synthesis and formation mechanism of porous silicon carbide stacked by nanoparticles from precipitated silica/glucose composites, J. Mater. Sci. 54 (2019) 2787–2795. https://doi.org/10.1007/s10853-018-3039-0.

[26] S. Kansal, P. Singh, S. Biswas, A. Chowdhury, D. Mandal, S. Priya, T. Singh, A. Chandra, Superior-catalytic performance of Ni–Co layered double hydroxide nanosheets for the reduction of p-nitrophenol, Int. J. Hydrogen Energy 48 (2023) 21372–21382. https://doi.org/10.1016/j.ijhydene.2022.04.213.

[27] G. Ghanashyam, H. Kyung Jeong, Flower-like molybdenum disulfide for efficient hydrogen and oxygen evolution reaction, Inorganica Chim. Acta 541 (2022) 121098. https://doi.org/10.1016/j.ica.2022.121098.

[28] J.A. Botas, D.P. Serrano, A. García, J. De Vicente, R. Ramos, Catalytic conversion of rapeseed oil into raw chemicals and fuels over Ni- and Mo-modified nanocrystalline ZSM-5 zeolite, Catal. Today 195 (2012) 59–70. https://doi.org/10.1016/j.cattod.2012.04.061.

[29] N. Asikin-Mijan, G. AbdulKareem-Alsultan, M.S. Mastuli, A. Salmiaton, M. Azuwa Mohamed, H. V. Lee, Y.H. Taufiq-Yap, Single-step catalytic deoxygenation-cracking of tung oil to bio-jet fuel over CoW/silica-alumina catalysts, Fuel 325 (2022) 124917. https://doi.org/10.1016/j.fuel.2022.124917.

[30] L.O.A. ROJAS, J.C. NASCIMENTO, J.A.C. RUIZ, M. BENACHOUR, J.F. SOUSA, Synthesis and Characterization of Bifunctional Transition-Metal/Silica-Alumina Catalysts for the Chloromethane Conversion To Hydrocarbons, Brazilian J. Pet. Gas 2 (2008) 154–166.

[31] M. Safa Gamal, N. Asikin-Mijan, M. Arumugam, U. Rashid, Y.H. Taufiq-Yap, Solvent-free catalytic deoxygenation of palm fatty acid distillate over cobalt and manganese supported on activated carbon originating from waste coconut shell, J. Anal. Appl. Pyrolysis 144 (2019) 104690. https://doi.org/10.1016/j.jaap.2019.104690.

[32] Z. He, X. Wang, Renewable energy and fuel production over transition metal oxides: The role of oxygen defects and acidity, Catal. Today 240 (2015) 220–228. https://doi.org/10.1016/j.cattod.2014.04.023.

[33] Z. Pan, R. Wang, M. Li, Y. Chu, J. Chen, Deoxygenation of methyl laurate to hydrocarbons on silica-supported Ni-Mo phosphides: Effect of calcination temperatures of precursor, J. Energy Chem. 24 (2015) 77–86. https://doi.org/10.1016/S2095-4956(15)60287-X.

[34] Z. Zhang, M. Tang, J. Chen, Effects of P/Ni ratio and Ni content on performance of γ-Al 2 O 3 -supported nickel phosphides for deoxygenation of methyl laurate to hydrocarbons, Appl. Surf. Sci. 360 (2016) 353–364. https://doi.org/10.1016/j.apsusc.2015.10.182.

[35] I. Shimada, S. Kato, N. Hirazawa, Y. Nakamura, H. Ohta, K. Suzuki, T. Takatsuka, Deoxygenation of triglycerides by catalytic cracking with enhanced hydrogen transfer activity, Ind. Eng. Chem. Res. 56

(2017) 75–86. https://doi.org/10.1021/acs.iecr.6b03514.

[36] J. Huang, W. Long, P.K. Agrawal, C.W. Jones, Effects of acidity on the conversion of the model bio-oil ketone cyclopentanone on H-Y zeolites, J. Phys. Chem. C 113 (2009) 16702–16710. https://doi.org/10.1021/jp905661w.

[37] X.Y. Guo, Y.Y. J., T.C. Li, Z.W. Ren, C.M. Yuan, Catalytic cracking of bio-oil from biomass pyrolysis, Chinese J. Process Eng. 3 (2011) 2539–2550.

[38] W. Kiatkittipong, S. Phimsen, K. Kiatkittipong, S. Wongsakulphasatch, N. Laosiripojana, S. Assabumrungrat, Diesel-like hydrocarbon production from hydroprocessing of relevant refining palm oil, Fuel Process. Technol. 116 (2013) 16–26. https://doi.org/10.1016/j.fuproc.2013.04.018.

[39] M. Snåre, I. Kubičková, P. Mäki-Arvela, K. Eränen, D.Y. Murzin, Heterogeneous catalytic deoxygenation of stearic acid for production of biodiesel, Ind. Eng. Chem. Res. 45 (2006) 5708–5715. https://doi.org/10.1021/ie060334i.

[40] D. Li, H. Xin, X. Du, X. Hao, Q. Liu, C. Hu, Recent advances for the production of hydrocarbon biofuel via deoxygenation progress, Sci. Bull. 60 (2015) 2096–2106. https://doi.org/10.1007/s11434-015-0971-0.

[41] A.T. Madsen, E.H. Ahmed, C.H. Christensen, R. Fehrmann, A. Riisager, Hydrodeoxygenation of waste fat for diesel production: Study on model feed with Pt/alumina catalyst, Fuel 90 (2011) 3433–3438. https://doi.org/10.1016/j.fuel.2011.06.005.

[42] S. Zulkepli, J.C. Juan, H.V. Lee, N.S.A. Rahman, P.L. Show, E.P. Ng, Modified mesoporous HMS supported Ni for deoxygenation of triolein into hydrocarbon-biofuel production, Energy Convers. Manag. 165 (2018) 495–508. https://doi.org/10.1016/j.enconman.2018.03.087.

[43] F. Mushtaq, R. Mat, F.N. Ani, Fuel production from microwave assisted pyrolysis of coal with carbon surfaces, Energy Convers. Manag. 110 (2016) 142–153. https://doi.org/10.1016/j.enconman.2015.12.008.

[44] M.S. Gamal, N. Asikin-Mijan, W.N.A.W. Khalit, M. Arumugam, S.M. Izham, Y.H. Taufiq-Yap, Effective catalytic deoxygenation of palm fatty acid distillate for green diesel production under hydrogen-free atmosphere over bimetallic catalyst CoMo supported on activated carbon, Fuel Process. Technol. 208 (2020). https://doi.org/10.1016/j.fuproc.2020.106519.

[45] P. Jiang, X. Wu, L. Zhu, F. Jin, J. Liu, T. Xia, T. Wang, Q. Li, Production of jet fuel range paraffins by low temperature polymerization of gaseous light olefins using ionic liquid, Energy Convers. Manag. 120 (2016) 338–345. https://doi.org/10.1016/j.enconman.2016.05.010.

[46] N. Asikin-Mijan, J.M. Ooi, G. AbdulKareem-Alsultan, H. V. Lee, M.S. Mastuli, N. Mansir, F.A. Alharthi, A.A. Alghamdi, Y.H. Taufiq-Yap, Free-H2 deoxygenation of Jatropha curcas oil into cleaner diesel-grade biofuel over coconut residue-derived activated carbon catalyst, J. Clean. Prod. 249 (2020) 119381. https://doi.org/10.1016/j.jclepro.2019.119381.

[47] D.M. Mason, The chemical reactor omnibook, 1st Editio, Chemical Engineering department, oregon state university, Corvallies, Oregon, 1980. https://doi.org/10.1016/0032-5910(80)85047-9.

[48] A. Ochoa, J. Bilbao, A.G. Gayubo, P. Castaño, Coke formation and deactivation during catalytic reforming of biomass and waste pyrolysis products: A review, Renew. Sustain. Energy Rev. 119 (2020). https://doi.org/10.1016/j.rser.2019.109600.

[49] F. Yang, H. Wang, J. Han, Q. Ge, X. Zhu, Enhanced selective deoxygenation of m-cresol to toluene on Ni/SiO2 catalysts derived from nickel phyllosilicate, Catal. Today 330 (2019) 149–156. https://doi.org/10.1016/j.cattod.2018.02.035.

[50] T. Danuthai, T. Sooknoi, S. Jongpatiwut, T. Rirksomboon, S. Osuwan, D.E. Resasco, Effect of extra-framework cesium on the deoxygenation of methylester over CsNaX zeolites, Appl. Catal. A Gen. 409–410 (2011) 74–81. https://doi.org/10.1016/j.apcata.2011.09.029.

[51] S. He, C. Sun, X. Yang, B. Wang, X. Dai, Z. Bai, Characterization of coke deposited on spent catalysts for long-chain-paraffin dehydrogenation, Chem. Eng. J. 163 (2010) 389–394. https://doi.org/10.1016/j.cej.2010.07.024.

[52] A.O. Adegbenjo, P.A. Olubambi, J.H. Potgieter, M.B. Shongwe, M. Ramakokovhu, Spark plasma sintering of graphitized multi-walled carbon nanotube reinforced Ti6Al4V, Mater. Des. 128 (2017) 119–129. https://doi.org/10.1016/j.matdes.2017.05.003.

[53] B. Zhang, Z. Zhong, T. Li, Z. Xue, X. Wang, R. Ruan, Biofuel production from distillers dried grains with solubles (DDGS) co-fed with waste agricultural plastic mulching films via microwave-assisted catalytic fast pyrolysis using microwave absorbent and hierarchical ZSM-5/MCM-41 catalyst, J. Anal. Appl. Pyrolysis 130 (2018) 249–255. https://doi.org/10.1016/j.jaap.2018.02.007.

[54] A.E. Barrón C., J.A. Melo-Banda, J.M. Dominguez E., E. Hernández M., R. Silva R., A.I. Reyes T., M.A. Meraz M., Catalytic hydrocracking of vegetable oil for agrofuels production using Ni-Mo, Ni-W, Pt and TFA catalysts supported on SBA-15, in: Catal. Today, 2011: pp. 102–110. https://doi.org/10.1016/j.cattod.2011.01.026.

[55] A. Niaei, D. Salari, J. Towfighi, P. Panahi, R. Nabavi, Effect of organophosphorous compounds as coke inhibitors on coking rate in the pyrolysis of naphtha, Pet. Sci. Technol. 26 (2008) 2170–2181. https://doi.org/10.1080/10916460701677906.

[56] M.D. Argyle, C.H. Bartholomew, Heterogeneous catalyst deactivation and regeneration: A review, Catalysts 5 (2015) 145–269. https://doi.org/10.3390/catal5010145.

List of supplementary (Figures)

1. Details product analysis in deoxygenated product from CoNiSi@Fe_3O_4 catalyzed DO PKO
2. Gas distribution by CoNiSi@Fe_3O_4 catalyzed DO PKO
3. Isotherm linear plot and pore distribution for fresh and used CoNiSi@Fe_3O_4 catalyst at DO reaction temperature 300, 330 and 350℃

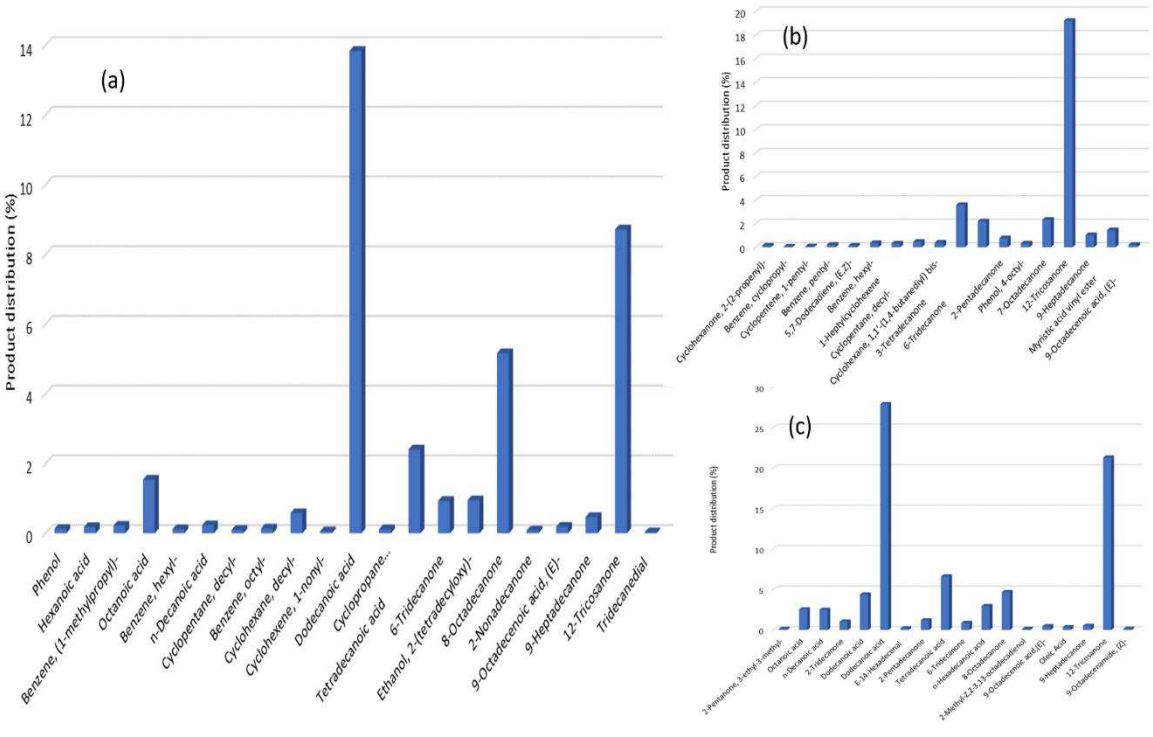


Fig. S1. Details product analysis in deoxygenated product from CoNiSi@Fe_3O_4 catalyzed DO PKO

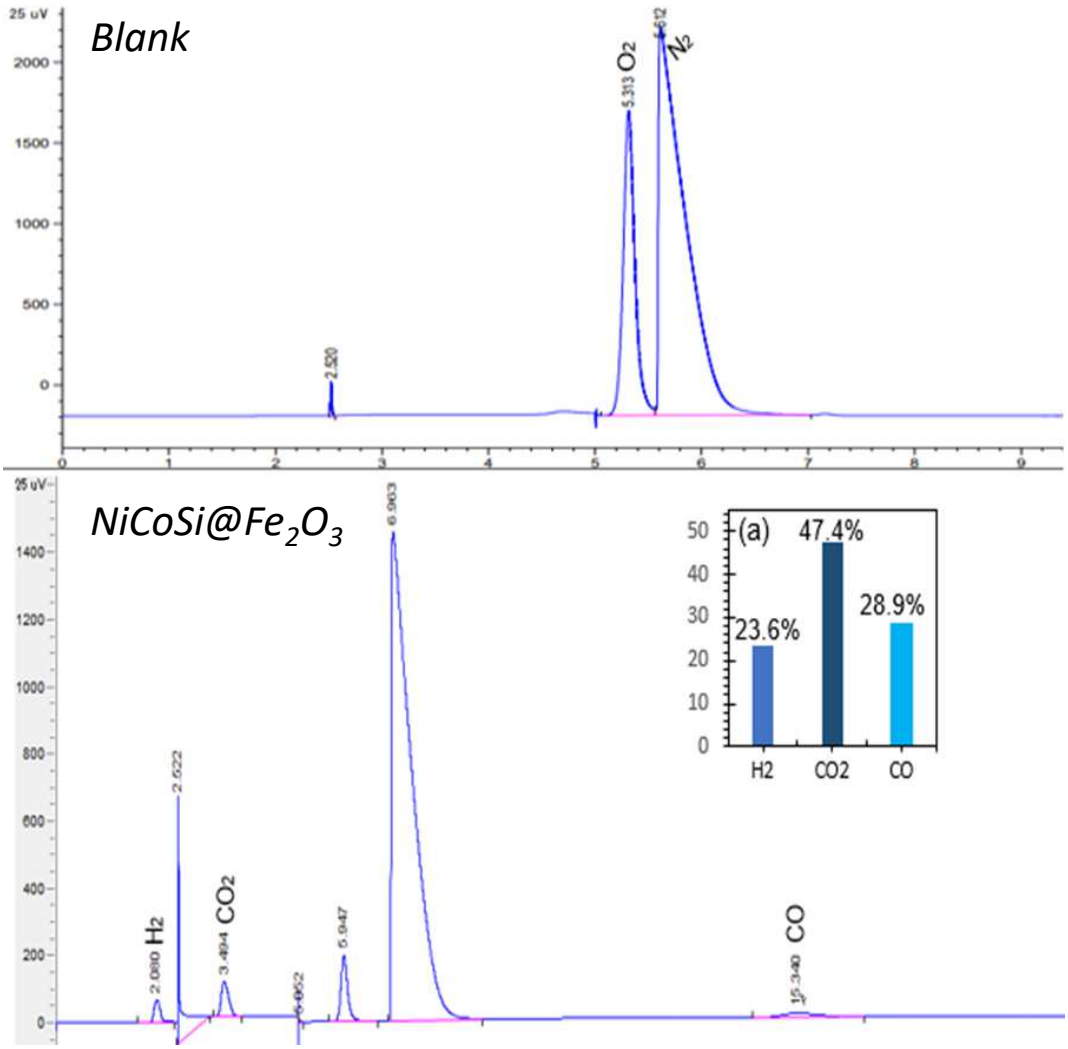


Fig. S2. Gas distribution by CoNiSi@Fe_3O_4 catalyzed DO PKO

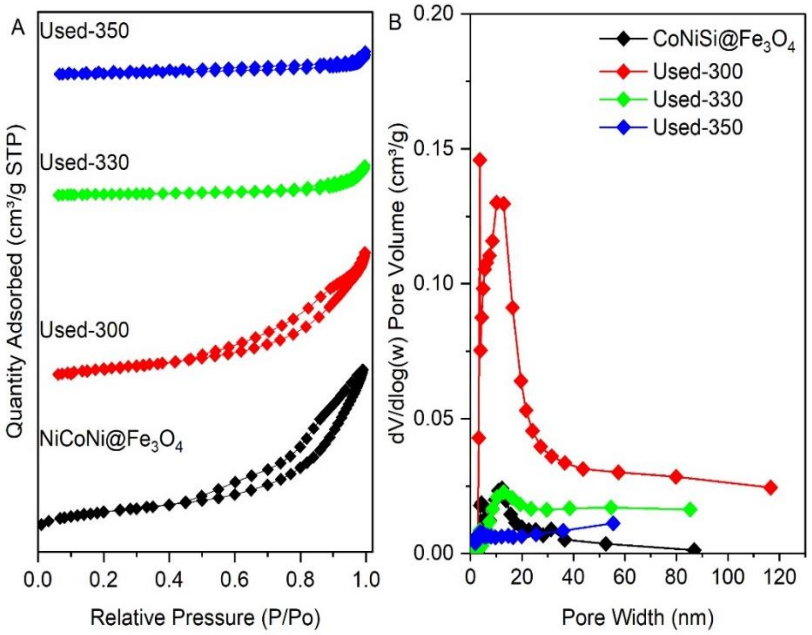


Fig. S3. isotherm linear plot and pore distribution for fresh and used CoNiSi@Fe_3O_4 catalyst at DO reaction temperature 300, 330 and 350℃